International Journal of Solids and Structures 294 (2024) 112763

Contents lists available at ScienceDirect

International Journal of Solids and Structures

journal homepage: www.elsevier.com/locate/ijsolstr

An in-plane phase-field ductile fracture model for orthotropic paperboard material

Alessandro Marengo [a], Umberto Perego [a,*], Eric Borgqvist [b], Johan Tryding [b,c], Matti Ristinmaa [c]

[a] Department of Civil and Environmental Engineering, Politecnico di Milano, P.zza L. da Vinci 32, 20133 Milan, Italy
[b] Tetra Pak, Ruben Rausings gata, 221 86 Lund, Sweden
[c] Division of Solid Mechanics, Lund University/LTH, P.O. Box 118, SE 221 00 Lund, Sweden

ARTICLE INFO

Keywords:
Phase field
Paperboard
Orthotropy
Effective stress
Ductile fracture

ABSTRACT

A phase-field ductile fracture formulation for orthotropic paperboard materials is proposed, based on an anisotropic, multi-surface elastoplastic model describing the in-plane behavior of paperboard. A variational statement for the finite-step elastoplastic problem is extended to include the variational description of Griffith-type brittle fracture by a phase-field gradient term. The interaction between plastic and fracture dissipation mechanisms is modeled by introducing a scalar modulation function, assuming plasticity driven damage growth. This function depends on a scalar measure of the plastic strain components in the material orthotropy frame. It modifies the fracture activation criterion in a non-variational fashion, resulting in a direction-dependent material strength against crack propagation. The model performance is assessed by comparing numerical simulations and experimental tests conducted in a climate-controlled laboratory.

1. Introduction

Paper and paperboard are easily recyclable artificial materials that can be produced at a low cost in huge amounts. For these reasons, the field of their possible applications is expanding, though the main application remains packaging. The global carton packaging market is rapidly growing, driven by increasing online transactions and the ensuing demand for recyclable packages. To reduce waste, carton packaging manufacturers have to use thinner and lighter weight grades of carton board, without compromising the safety and quality of the packaging. During the package forming process, the package undergoes converting and filling procedures that severely stress the material. The combination of growing competition and more severe regulations is forcing the packaging companies to fully exploit the mechanical properties of paperboard, which is the material providing the mechanical strength to the final product, minimizing manufacturing defects.

Paperboard is a multi-scale material, composed of wood-fibers that are mainly arranged into planes stacked one onto the other. The manufacturing process of the blank paperboard sheet induces an in-plane preferential orientation of the fibers. Two in-plane material directions can be recognized: the Machine Direction (MD) and the Cross machine Direction (CD). The presence of multiple plies of fibers entails a high degree of anisotropy between the in-plane and the out-of-plane (ZD) directions of the paper sheet. As a result, paperboard is an orthotropic material, with relatively mild in-plane anisotropy in MD and CD and strong anisotropy in out-of-plane ZD (Mäkelä and Östlund, 2003; Borgqvist et al., 2014, 2015).

A recent review of state-of-the-art approaches for paper modeling can be found in Simon (2021), where models addressing the multi-scale and multi-physics nature of paperboard have been extensively reviewed. Paper models at the fiber scale can be further subdivided into models focusing on the single fiber behavior, on the fiber–fiber bonds and on the fiber network scale (Simon, 2021). In the present work, the focus is on paperboard behavior at the sheet scale, where paperboard can be considered a homogeneous, orthotropic material, whose behavior can be described by means of continuum mechanics models. In most paperboard models at this scale (Borgqvist et al., 2015, 2016), the hypothesis of decoupled in-plane and out-of-plane behavior is assumed. This is justified by the experimental evidence that the out-of-plane Poisson ratio is nearly zero (Stenberg and Fellers, 2002). Paperboard shows a highly nonlinear response already under small loading. Furthermore, under loading–unloading cycles in the nonlinear regime it exhibits evident non-recoverable strains, revealing the elastoplastic nature of its pre-failure behavior and motivating the use of elastoplastic models for its description (Harrysson and Ristinmaa, 2008).

* Corresponding author.
E-mail addresses: alessandro.marengo@polimi.it (A. Marengo), umberto.perego@polimi.it (U. Perego), Eric.Borgqvist@tetrapak.com (E. Borgqvist), Johan.Tryding@tetrapak.com (J. Tryding), matti.ristinmaa@solid.lth.se (M. Ristinmaa).

https://doi.org/10.1016/j.ijsolstr.2024.112763
Received 7 July 2023; Received in revised form 7 March 2024; Accepted 8 March 2024
Available online 15 March 2024

The possibility of obtaining acceptable, first-hand simulations of paperboard response during converting procedures, using only features already available in a commercial code, has been investigated, e.g., in Domaneschi et al. (2017). An elastoplastic model, with cohesive interfaces through the thickness, has been first proposed in Nygårds et al. (2005) and Nygårds et al. (2009) to simulate delamination. Addressing the problem of large-scale forming simulations, an interface crease element, accounting for elasto-plasticity and damage, has been interposed between shell elements of the Mindlin–Reissner type (Giampieri et al., 2011). An in-plane orthotropic elastoplastic model of paperboard with multiple yield modes has been proposed by Xia et al. (2002). It is able to distinguish between yielding in tension and compression along the different material directions, while the out-of-plane response is treated as elastic. An application to non-isotropic hardening plasticity has been presented in Borgqvist et al. (2014), where the different in-plane yield mechanisms present a coupled hardening behavior. Xia's formulation has been subsequently extended including a description of the nonlinear out-of-plane behavior to capture the material response during converting to package material. Then, the yield criterion has been enhanced to include the additional yield mechanisms characterizing the out-of-plane response (Borgqvist et al., 2015, 2016; Robertsson et al., 2018). These latter models, however, did not account for material degradation and crack nucleation and propagation. The importance of nonlocal damage modeling in random fiber networks has been addressed in Isaksson and Hägglund (2009), while the damage localization bandwidth has been shown to be related to the fiber average length in Niskanen et al. (2001). Experimental tests to characterize damage onset and propagation in isotropic paper sheets have been presented in Isaksson et al. (2006), suggesting that a nonlocal isotropic scalar damage model has to be used in the analysis, due to the presence of high stress gradients generated when the main damage mechanism is fiber bonds failure. A nonlocal anisotropic elastoplastic damage model with two damage variables, for orthotropic paperboard has been proposed in Isaksson et al. (2004), where three scalar internal variables have been introduced to capture material failure in the directions of orthotropy MD, CD, and ZD. Here, damage irreversibility has been enforced, a unique internal length parameter governs the nonlocal model and only the elastic free energy is degraded by damage. The idea of a damage variable associated with each set of fibers in a fiber network can also be found in Chen and Silberstein (2019).

A phase-field modeling of brittle fracture has been proposed in Bourdin et al. (2000) as the topological regularization of the sharp crack variational formulation of Griffith-type fracture (Francfort and Marigo, 1998). The regularization of the sharp topology requires the introduction of a regularization parameter, i.e., an internal length, measuring the portion of the solid domain where the crack has been smeared. The scalar phase-field d is employed as an order parameter and, from a mechanical standpoint, it can be interpreted as a damage variable since it is interpolating the unbroken ($d = 0$) and the fully-broken ($d = 1$) material states. Likewise, the internal length can be interpreted as a measure of the damage localization bandwidth. The solution to a boundary value problem in terms of displacements and phase-field variables is obtained from a constrained minimization principle, where the constraint on the phase-field growth derives from the irreversibility of the crack evolution process. The issue of irreversibility has been addressed with various approaches, either variationally non-consistent, like the *history variable* (Miehe et al., 2010), or variationally consistent, like the penalty method (Gerasimov and De Lorenzis, 2019) and the Projected Successive Over-Relaxation (Marengo et al., 2021), allowing for a rigorous enforcement of the constraint.

The extension of the phase-field formulation to ductile media is less straightforward, since a variational formulation of ductile fracture is missing (Ambati et al., 2015). A review of different approaches can be found in Alessi et al. (2018a) and Marengo and Perego (2023a). In the current work, the attention is focused on the *effective stress* approach (see, e.g., Ulloa et al. (2016), Miehe et al. (2017), Choo and Sun (2018), Huang and Gao (2019), Wambacq et al. (2021) and Marengo and Perego (2023b)), combined with an AT1 (Ambrosio and Tortorelli, 1990) phase-field dissipation model (see, e.g., Alessi et al. (2018b), Samaniego et al. (2021), Hu et al. (2021), Talamini et al. (2021), Wambacq et al. (2021) and Marengo and Perego (2023b)). The effective stress is defined as the true stress acting on the continuous part of the damaged material. The main consequence of this approach is the material continuing to yield after damage initiation. The AT1 formulation implies the presence of a threshold in the damage activation criterion, allowing for a purely elastic or elastoplastic regime before crack initiation.

The orthotropic nature of paperboard also requires to be taken into account in the phase-field formulation, since orthotropy affects both the elastoplastic behavior and the fracture evolution. An orthotropic finite elasticity model has been coupled with a phase-field brittle model in Raina and Miehe (2016), to model crack propagation in biological tissues, with an isotropic fracture dissipation and a driving force modified in a non-variational fashion. A principal stress activation criterion has been postulated where only positive principal stresses are assumed to contribute to crack propagation, and a structural tensor to account for material orientation in the damage activation criterion. A structural tensor is usually introduced in the phase-field gradient term (see, e.g., Teichtmeister et al. (2017), Quintanas-Corominas et al. (2019), Li and Maurini (2019) and Dean et al. (2020)) to make the fracture dissipation dependent on orthotropy directions, to induce an orientation dependent toughness. An orthotropic elastic energy is also generally employed (see, e.g., Teichtmeister et al. (2017), Quintanas-Corominas et al. (2019) and Dean et al. (2020)). The energy split to allow for the promotion of crack onset and propagation only in tensile-dominated portions of the domain is addressed in Teichtmeister et al. (2017) by means of an energetic approach, using the complementary energy, or a stress criterion (see also Raina and Miehe (2016)). Both approaches rely on the spectral decomposition of the effective stress tensor. A different approach consists of postulating the existence of multiple failure mechanisms associated with multiple damage variables (Bleyer and Alessi, 2018). An extension of orthotropic phase-field fracture to elastoplastic materials has been proposed in Dean et al. (2020), where the orthotropic behavior is considered in the elastic energy, in the volumetric-dependent yield criterion, and in the fracture energy via a structural tensor approach.

The phase-field approach to fracture brings several important theoretical advantages. It is based on a rigorous variational formulation, exhibiting features, among others, that allow discussing the existence of solutions and studying the asymptotic Γ-convergence behavior of the dissipated energy. From the computational point of view, the variational nature of phase-field formulations naturally suggests a staggered, alternate minimization algorithm for the problem solution. This has the advantage that the momentum balance equation can be solved using the standard Newton–Raphson algorithm with the elastoplastic tangent, which does not need to be modified with respect to the elastoplastic problem without damage. All these properties give rise to solution algorithms that have proven to be extremely robust and computationally effective over the years.

The present work uses a unique scalar damage variable to model the in-plane crack evolution based on the fiber-debonding nature of fracture initiation (see Isaksson et al. (2006)), and, in this respect, it is simpler than other nonlocal anisotropic damage models that make use of two damage variables to model anisotropy (see, e.g. Isaksson et al. (2004)). To account for the anisotropic development of damage, a plasticity-driven damage activation criterion is formulated, whereby damage can initiate only when a suitable amount of plastic dissipation has been achieved. In this way, the anisotropic damage evolution is a consequence of the anisotropic plasticity model, and scalar damage can be used to model degradation in the different material directions. The complex interaction between ductile and brittle dissipation

mechanisms is modeled by considering a non-variational modification of the brittle fracture dissipation term, in line with what has been proposed by several other authors (see Huang and Gao (2019), Yin and Kaliske (2020), Hu et al. (2021) and Marengo and Perego (2023b)). Following Ortiz and Martin (1989), Simo and Honein (1990), Comi et al. (1992), Corigliano (1994) and Comi and Perego (1995), a finite-step variational formulation of the elastoplastic problem is considered, and the fracture behavior is accounted for by including the brittle fracture dissipation energy in the elastoplastic finite-step energy functional. This new term is then modified in a non-variational fashion to capture the competition between the plastic and brittle dissipation mechanisms (Huang and Gao, 2019; Yin and Kaliske, 2020; Hu et al., 2021; Marengo and Perego, 2023b), allowing damage to evolve only after enough plastic dissipation has taken place. Following Marengo and Perego (2023b), the modification consists of enriching the critical energy release rate functional by a scalar coupling term, named modulation function, which models the plasticity-driven crack nucleation and propagation by modulating the material toughness. To account for the material anisotropy, the modulation function is made to depend upon a directional scalar measure of the plastic deformation ξ. When ξ reaches a prescribed limit value, the modulation function vanishes and the original variational structure of the problem is recovered in the final stage of failure. A directional activation criterion for damage is introduced in the plastic strain space, similar to Raina and Miehe (2016) but using Xia's yield function (Xia et al., 2002) as the yield criterion. The plastic strain measure ξ defines the *distance* of the current plastic deformation state from the limit surface for damage activation in the plastic strain space.

This work is intended to model crack propagation in 2D boards, typically promoted by tensile stress states. Since no crack propagation is expected in 2D compression, the model does not consider damage propagation in compression. On the other hand, compression states may produce damage in localized bands and delamination, which, however, is an out-of-plane mechanism not considered in this work (see, e.g., Borgqvist et al. (2016)). To prevent damage evolution in compression, the definition of the directional plastic strain measure ξ considers only the positive part of normal plastic strain components in the material orthotropy directions, and the energy split, usually introduced to avoid damage propagation under prevailing compression states, becomes unnecessary.

Section 2 outlines a finite-step variational formulation that applies to general orthotropic ductile materials. In Section 3, the fracture activation criterion is modified by introducing the modulation function and its plastic strain measure. Section 4 presents the finite element discretization of the governing equations and the solution strategy based on a staggered algorithm is outlined. In Section 5 the results of numerical simulations and experimental tests are compared to assess the predictive capability of the model. Finally, conclusions are drawn in Section 6.

2. Phase-field ductile fracture of orthotropic materials

2.1. Nominal & effective responses

Let $\Omega \subset \mathbb{R}^{n_{dim}}$ be the undeformed and undamaged domain, n_{dim} being the problem dimension. It is subject to Dirichlet boundary conditions on $\partial\Omega_D$ and Neumann boundary conditions on $\partial\Omega_N$, with $\partial\Omega_D \cup \partial\Omega_N = \partial\Omega$ and $\partial\Omega_D \cap \partial\Omega_N = \emptyset$. The vector displacement field $\mathbf{u}$ is subject to $\mathbf{u} = \mathbf{u}_D$ on $\partial\Omega_D$. The scalar phase-field (damage-like) variable d ranges from 0 to 1, interpolating the unbroken and fully broken state of the material, respectively. The material degradation function $\omega(d)$ accounts for the presence of damage in the material bulk and it has the properties $\omega(0) = 1$, $\omega(1) = 0$ and $\omega'(d) < 0$. In the damaged state, $d\Omega$ defines the infinitesimal nominal volume, equal to the original undamaged volume, while $d\widetilde{\Omega} = \omega\, d\Omega$ is the current effective volume, i.e., the nominal volume minus a measure of the volume of micro-voids due to damage. In what follows, Ω denotes the nominal volume and $\widetilde{\Omega}$ the effective one. The effective quantities, denoted by a superposed tilde $\widetilde{(\cdot)}$, represent the damaged volume. In contrast, quantities without a tilde are nominal quantities and refer to the reference volume. The pointwise transformation from effective to nominal quantity reads:

$$\underbrace{\widetilde{(\cdot)}}_{effective}\ \underbrace{d\widetilde{\Omega}}_{effective} = \underbrace{\widetilde{(\cdot)}}_{effective}\ \omega\ \underbrace{d\Omega}_{nominal} = \underbrace{(\cdot)}_{nominal}\ \underbrace{d\Omega}_{nominal} \tag{1}$$

2.2. State variables & evolution laws

Making reference to an elastoplastic material, belonging to the class of *generalized standard materials* (Halphen and Son, 1975), i.e. endowed with convex free energy density and yield function with associative evolution of plastic strains and kinematic internal variables, the considered state variables are the total strain tensor $\boldsymbol{\varepsilon} := \boldsymbol{\nabla}^s\mathbf{u}$, where $\boldsymbol{\nabla}^s(\cdot)$ represents the symmetric gradient operator, the plastic strain tensor $\boldsymbol{\varepsilon}^p$, a set of hardening internal variables of kinematic nature cast in the vector $\boldsymbol{\beta}$, and the damage-like phase field d. The nominal free energy density ψ is assumed to be additively decomposed into its elastic (reversible) part $\omega\,\widetilde{\psi}^e(\boldsymbol{\varepsilon}^e)$, $\boldsymbol{\varepsilon}^e = \boldsymbol{\varepsilon} - \boldsymbol{\varepsilon}^p$ denoting the elastic strain tensor, and hardening (unrecoverable) $\omega\,\widetilde{\psi}^p(\boldsymbol{\beta})$ part, the latter associated with the internal elastic energy stored in the material because of irreversible deformations of the microstructure. The energies $\widetilde{\psi}^e(\boldsymbol{\varepsilon}^e)$ and $\widetilde{\psi}^p(\boldsymbol{\beta})$, assumed to be convex functions of their arguments, are the undamaged or *effective* elastic and hardening free energy densities. The *nominal* and *effective* free energies are defined as:

$$\psi := \omega\,\widetilde{\psi} \quad , \quad \widetilde{\psi} := \widetilde{\psi}^e + \widetilde{\psi}^p \tag{2}$$

According to the Clausius–Duhem dissipation inequality, the nominal specific dissipation rate ϕ must be non-decreasing in any transformation, i.e. $\phi := \boldsymbol{\sigma} : \dot{\boldsymbol{\varepsilon}} - \dot{\psi} \geq 0$, where $\boldsymbol{\sigma}$ is the Cauchy stress tensor, $\dot{\boldsymbol{\varepsilon}}$ is the total strain rate, and $\dot{\psi}$ is the free energy rate. Introducing the expression (2) into the dissipation inequality gives:

$$\phi := \boldsymbol{\sigma} : \dot{\boldsymbol{\varepsilon}} - \dot{\psi} = \underbrace{\left(\boldsymbol{\sigma} - \omega\,\partial_{\boldsymbol{\varepsilon}^e}\widetilde{\psi}^e\right) : \dot{\boldsymbol{\varepsilon}}^e}_{elastic} + \underbrace{\boldsymbol{\sigma} : \dot{\boldsymbol{\varepsilon}}^p - \omega\,\partial_{\boldsymbol{\beta}}\widetilde{\psi}^p \cdot \dot{\boldsymbol{\beta}}}_{plastic} - \underbrace{\omega'\,\widetilde{\psi}\,\dot{d}}_{fracture} \geq 0 \tag{3}$$

Using standard arguments, the nominal and effective elastic evolution laws

$$\boldsymbol{\sigma} = \omega\,\widetilde{\boldsymbol{\sigma}} \ , \quad \widetilde{\boldsymbol{\sigma}} := \partial_{\boldsymbol{\varepsilon}^e}\widetilde{\psi}^e \tag{4}$$

and the nominal and effective dissipation rate due to plasticity only, ϕ^p and $\widetilde{\phi}^p$

$$\phi^p = \omega\,\widetilde{\phi}^p \ , \quad \widetilde{\phi}^p := \widetilde{\boldsymbol{\sigma}} : \dot{\boldsymbol{\varepsilon}}^p - \widetilde{\boldsymbol{\chi}} \cdot \dot{\boldsymbol{\beta}} \geq 0 \tag{5}$$

are obtained from the dissipation inequality, $\widetilde{\boldsymbol{\chi}}$ being the vector of effective hardening variables gathering the thermodynamic forces work-conjugated to the internal variables $\boldsymbol{\beta}$. From (3), $\boldsymbol{\chi}$ and $\widetilde{\boldsymbol{\chi}}$ turn out to be defined as:

$$\boldsymbol{\chi} = \omega\widetilde{\boldsymbol{\chi}} \ , \quad \widetilde{\boldsymbol{\chi}} := \partial_{\boldsymbol{\beta}}\widetilde{\psi}^p \tag{6}$$

Effective stresses and static hardening parameters $(\widetilde{\boldsymbol{\sigma}}, \widetilde{\boldsymbol{\chi}})$ have to satisfy the yield condition

$$f_y(\widetilde{\boldsymbol{\sigma}}, \widetilde{\boldsymbol{\chi}}) \leq 0 \tag{7}$$

where f_y is the yield function, convex in the space of stress and static internal variables. Since only the effective part of the volume experiences plastic deformations, the yield criterion is expressed in terms of effective stresses and static internal variables. The effective elastoplastic evolution laws are derived from the stationarity conditions for the effective principle of maximum dissipation. Accordingly, the dissipation in (3) is maximized with respect to admissible effective

stresses $\widetilde{\boldsymbol{\sigma}}$ and static hardening parameters $\widetilde{\boldsymbol{\chi}}$, i.e., under the constraints given by condition (7):

$$\dot{\boldsymbol{\varepsilon}}^p = \dot{\lambda}\,\partial_{\widetilde{\boldsymbol{\sigma}}} f_y \quad , \quad \dot{\boldsymbol{\beta}} = -\dot{\lambda}\,\partial_{\widetilde{\boldsymbol{\chi}}} f_y \quad , \quad \dot{\lambda} \geq 0 \quad , \quad f_y \leq 0 \quad , \quad \dot{\lambda}\, f_y = 0 \tag{8}$$

where $\dot{\lambda}$ is the non-negative rate of a scalar plastic multiplier. Finally, from (3) the specific effective dissipation rate $\dot{\phi}$ is rewritten as:

$$\dot{\phi} := \omega\,\dot{\widetilde{\phi}}^p + \dot{\phi}^f \quad , \quad \dot{\phi}^f := G\,\dot{d} \quad , \quad G := -\omega'\,\widetilde{\psi} \tag{9}$$

where $\dot{\phi}^f$ is the specific brittle fracture dissipation rate. G is the strain energy release rate, i.e., the specific free energy released upon a unit damage growth.

2.3. Variational formulation of the finite-step problem

2.3.1. Phase-field finite-step variational formulation of ductile fracture

A finite time-step increment is considered. The initial and final times of the step are t^n and t^{n+1}, respectively. Therefore, the time increment in the current step is $\Delta t = t^{n+1} - t^n$. The increment of a generic quantity is denoted by $\Delta(\cdot) = (\cdot) - (\cdot)_n$, where $(\cdot)$ represents quantities evaluated at time t^{n+1} and $(\cdot)_n$ represents quantities evaluated at time t^n. For notation convenience, the $n+1$ exponent will be omitted for all quantities evaluated at t^{n+1}. An Euler backward return mapping scheme is assumed for the time integration of the elastoplastic law in rate form. The solution of the finite-step problem is expressed in terms of the following set of independent fields

$$S := (\mathbf{u}, \boldsymbol{\varepsilon}, \Delta\boldsymbol{\varepsilon}^p, \widetilde{\boldsymbol{\sigma}}, \widetilde{\boldsymbol{\sigma}}^p, \widetilde{\boldsymbol{\chi}}, \Delta\boldsymbol{\beta}, \Delta\lambda, \Delta d) \tag{10}$$

The stress field $\widetilde{\boldsymbol{\sigma}}$ in S now plays the role of a Lagrange multiplier used for the weak enforcement of compatibility, while the effective stress $\widetilde{\boldsymbol{\sigma}}$ in the plastic dissipation increment (5) and in the yield condition (7) is denoted by $\widetilde{\boldsymbol{\sigma}}^p$ in the equation below. Following classical variational formulations of the finite-step elastoplastic problem (see, e.g., Simo and Honein (1990) and Comi and Perego (1995)), the solution can be given a variational characterization by showing that the equations governing the ductile–brittle finite-step problem coincide with the stationarity conditions of the following Lagrangian functional (Marengo and Perego, 2023b)

$$\begin{aligned}
\mathcal{L}^n(S) := & \underbrace{\int_\Omega \omega(d)\left[\widetilde{\psi}^e(\boldsymbol{\varepsilon} - \boldsymbol{\varepsilon}^{p\,n} - \Delta\boldsymbol{\varepsilon}^p) + \widetilde{\psi}^p(\boldsymbol{\beta}^n + \Delta\boldsymbol{\beta})\right] \mathrm{d}\Omega}_{\text{stored internal energy}} \\
& - \underbrace{\int_\Omega \mathbf{b}\cdot\mathbf{u}\,\mathrm{d}\Omega - \int_{\partial\Omega_N} \mathbf{t}\cdot\mathbf{u}\,\mathrm{d}\Gamma}_{\text{external work}} \\
& + \underbrace{\int_\Omega \omega(d)\left(\widetilde{\boldsymbol{\sigma}}^p : \Delta\boldsymbol{\varepsilon}^p - \widetilde{\boldsymbol{\chi}}\cdot\Delta\boldsymbol{\beta}\right)\mathrm{d}\Omega}_{\text{plastic dissipation increment}} + \underbrace{\int_\Omega \phi^f(d,\nabla d)\,\mathrm{d}\Omega}_{\text{fracture energy}} \\
& + \underbrace{\int_\Omega \frac{\eta_f}{2\Delta t}\left(\Delta d\right)^2 \mathrm{d}\Omega}_{\text{viscous energy}} \\
& + \underbrace{\int_\Omega \omega(d)\,\widetilde{\boldsymbol{\sigma}} : (\nabla^s\mathbf{u} - \boldsymbol{\varepsilon})\,\mathrm{d}\Omega}_{\text{compatibility constraint}} - \underbrace{\int_\Omega \omega(d)\,\Delta\lambda\, f_y(\widetilde{\boldsymbol{\sigma}}^p, \widetilde{\boldsymbol{\chi}})\,\mathrm{d}\Omega}_{\text{plastic admissibility}}
\end{aligned} \tag{11}$$

subject to

$$\Delta\lambda \geq 0, \quad \Delta d \geq 0, \quad \mathbf{u} = \mathbf{u}_D \text{ on } \partial\Omega_D \tag{12}$$

where the superscript n of $\mathcal{L}^n(S)$ implies that the irreversible quantities $\boldsymbol{\varepsilon}^{p\,n}$, $\boldsymbol{\beta}^n$ and d^n at the end of the previous time step are fixed parameters in the optimization procedure.

While the fracture energy and the external work are defined on the reference nominal volume Ω, the other integrals in (11) are defined on the effective portion $\widetilde{\Omega}$ of the material volume. These integrals are then transformed in (11) into integrals over the nominal volume by using $\int_{\widetilde{\Omega}} \widetilde{(\cdot)}\,\mathrm{d}\widetilde{\Omega} = \int_\Omega \omega\,\widetilde{(\cdot)}\,\mathrm{d}\Omega$. The vectors $\mathbf{b}$ and $\mathbf{t}$ are the body forces and the surface tractions, respectively. In the standard phase-field formulation, one has

$$\phi^f(d, \nabla d) = w(d) + {}^1\!/_2\, c_d\, \nabla d\cdot\nabla d \tag{13}$$

where $w(d)$ is the local part of the phase-field specific dissipation. The constant parameter c_d measures the damage diffusion bandwidth and is related to the fracture internal length l_{0d}. The viscous coefficient η_f in (11) introduces a pseudo-time measure of the crack propagation rate. This dissipative term is introduced for algorithmic reasons, to facilitate convergence in the softening branch of the response curve, when this is particularly brittle. The equations and inequalities governing the considered finite-step ductile fracture boundary value problem are obtained as stationarity conditions of $\mathcal{L}^n(S)$ with respect to variations of the fields in S, in the sense of variational inequalities, due to the inequality constraints on $\Delta\lambda$ and Δd (see Marengo and Perego (2023a) for details).

2.3.2. Governing equations of the non-local problem

As in standard compatible finite elements, the compatibility condition is satisfied in strong form by assuming $\boldsymbol{\varepsilon} = \boldsymbol{\nabla}_s\mathbf{u}$. The weak form of the momentum balance equation, expressed in terms of nominal quantities, reads:

$$\int_\Omega \omega\,\widetilde{\boldsymbol{\sigma}} : \delta\boldsymbol{\varepsilon}\,\mathrm{d}\Omega = \int_\Omega \mathbf{b}\cdot\delta\mathbf{u}\,\mathrm{d}\Omega + \int_{\partial\Omega_N} \mathbf{t}\cdot\delta\mathbf{u}\,\mathrm{d}\Gamma \tag{14}$$

The effective state equations and elastoplastic finite-step evolution laws are given by:

$$\widetilde{\boldsymbol{\sigma}} = \partial_{\boldsymbol{\varepsilon}}\widetilde{\psi}^e \quad , \quad \widetilde{\boldsymbol{\chi}} = \partial_{\boldsymbol{\beta}}\widetilde{\psi}^p \quad , \quad \Delta\boldsymbol{\varepsilon}^p = \Delta\lambda\,\partial_{\widetilde{\boldsymbol{\sigma}}} f_y \quad , \quad \Delta\boldsymbol{\beta} = -\Delta\lambda\,\partial_{\widetilde{\boldsymbol{\chi}}} f_y \tag{15}$$

where the derivatives of $\widetilde{\psi}^e$, $\widetilde{\psi}^p$ and f_y are evaluated at the final instant of the time step.

The variational inequalities arising from constrained variations of $\Delta\lambda$ can be cast in the form of Kuhn–Tucker conditions:

$$\Delta\lambda \geq 0 \quad , \quad f_y(\widetilde{\boldsymbol{\sigma}}, \widetilde{\boldsymbol{\chi}}) \leq 0 \quad , \quad f_y(\widetilde{\boldsymbol{\sigma}}, \widetilde{\boldsymbol{\chi}})\,\Delta\lambda = 0 \tag{16}$$

Defining the driving energy density $\hat{\widetilde{\psi}}$,

$$\hat{\widetilde{\psi}}(\boldsymbol{\varepsilon}, \boldsymbol{\varepsilon}^p, \widetilde{\boldsymbol{\sigma}}, \widetilde{\boldsymbol{\chi}}, \boldsymbol{\beta}) := \widetilde{\psi}(\boldsymbol{\varepsilon}, \boldsymbol{\varepsilon}^p, \boldsymbol{\beta}) + \Delta\widetilde{\phi}^p(\boldsymbol{\varepsilon}^p, \widetilde{\boldsymbol{\sigma}}, \widetilde{\boldsymbol{\chi}}, \boldsymbol{\beta}) \tag{17}$$

and the energy release rate $\mathcal{G}$ and the critical energy release rate $\mathcal{G}_c$ functionals,

$$\mathcal{G}(\boldsymbol{\varepsilon}, \boldsymbol{\varepsilon}^p, \boldsymbol{\beta}, d)[\delta d] := -\int_\Omega \omega'(d)\,\hat{\widetilde{\psi}}(\boldsymbol{\varepsilon}, \boldsymbol{\varepsilon}^p, \boldsymbol{\beta})\,\delta d\,\mathrm{d}\Omega \tag{18a}$$

$$\mathcal{G}_c(d)[\delta d] := \int_\Omega \left\{ \left[w'(d) + \frac{\eta_f}{\Delta t}\Delta d \right] \delta d + c_d\,\nabla d\cdot\nabla\delta d \right\} \mathrm{d}\Omega \tag{18b}$$

the non-local damage activation conditions for elastoplastic fracture arising from constrained variations of Δd are written in equivalent Kuhn–Tucker form as:

$$\Delta d \geq 0 \quad , \quad \mathcal{F}_d(\boldsymbol{\varepsilon}, \boldsymbol{\varepsilon}^p, \boldsymbol{\beta}, d) \leq 0 \quad , \quad \mathcal{F}_d(\boldsymbol{\varepsilon}, \boldsymbol{\varepsilon}^p, \boldsymbol{\beta}, d)[\Delta d] = 0 \tag{19}$$

where $\mathcal{F}_d$ is a non-local fracture activation functional defined as:

$$\mathcal{F}_d(\boldsymbol{\varepsilon}, \boldsymbol{\varepsilon}^p, \boldsymbol{\beta}, d)[\delta d] := \Big(\mathcal{G}(\boldsymbol{\varepsilon}, \boldsymbol{\varepsilon}^p, \boldsymbol{\beta}, d) - \mathcal{G}_c(d)\Big)[\delta d] \tag{20}$$

2.4. Constitutive assumptions

For the implementation considered in this work, the general framework described so far is restricted to the in-plane behavior of paperboard. An orthotropic elastoplastic behavior is assumed. The two in-plane material directions are the Machine-Direction (MD) and Cross machine-Direction (CD), and they will be denoted with the subscripts 1 and 2 respectively.

2.4.1. In-plane orthotropic elastoplasticity for paperboard

The elastic free energy is expressed in the form:

$$\widetilde{\psi}^e(\boldsymbol{\varepsilon}-\boldsymbol{\varepsilon}^p) := \frac{1}{2}(\boldsymbol{\varepsilon}-\boldsymbol{\varepsilon}^p) : \widetilde{\mathbb{D}} : (\boldsymbol{\varepsilon}-\boldsymbol{\varepsilon}^p) \tag{21}$$

where $\widetilde{\mathbb{D}}$ is the tensor of effective orthotropic elastic moduli. Among the several available in-plane elastoplastic models for paperboard (see Simon (2021) for a recent review), the material has been assumed to obey the Xia yield criterion (Xia et al., 2002):

$$f_y(\widetilde{\boldsymbol{\sigma}},\widetilde{\chi}) = \sum_{s=1}^{6}\left[\left(\frac{\langle\sigma_n^{(s)}(\widetilde{\boldsymbol{\sigma}})\rangle_+}{\sigma_y^{(s)}(\widetilde{\chi})}\right)^{2k}\right] - 1 \tag{22}$$

where s denotes the sth yield mechanism. The possible yield mechanisms are MD tension ($s=1$), CD tension ($s=2$), positive shear ($s=3$), MD compression ($s=4$), CD compression ($s=5$), and negative shear ($s=6$). For each mechanism, the normal stress $\sigma_n^{(s)}(\widetilde{\boldsymbol{\sigma}}) := \widetilde{\boldsymbol{\sigma}} : \mathbb{n}^{(s)}$ is defined as the projection of the stress tensor along the sth unit normal $\mathbf{n}^{(s)}$ to the yield surface and $\mathbb{n}^{(s)} = \mathbf{n}^{(s)} \otimes \mathbf{n}^{(s)}$. The normal vectors $\mathbf{n}^{(s)}$ are material parameters. The sth mechanism contributes to the summation in the yield function only if $\sigma_n^{(s)} > 0$ thanks to the positive Macaulay bracket $\langle\sigma_n^{(s)}\rangle_+$. The hardening mechanisms are assumed to be uncoupled and the effective yield stress reads $\sigma_y^{(s)}(\widetilde{\chi}) = \bar{\sigma}_y^{(s)} + \widetilde{\chi}^{(s)}$, where $\bar{\sigma}_y^{(s)}$ is the initial effective yield stress. Finally, the exponent k governs the degree of interaction between the different mechanisms. For $k \to \infty$, the yields surface is a polyhedron in stress space, while for $k=1$ it becomes an ellipsoid in the space of the three independent stress components. The static hardening variables $\widetilde{\chi}^{(s)}$ evolve according to the logarithmic law (Borgqvist et al., 2014, 2015):

$$\widetilde{\chi}^{(s)}(\beta^{(s)}) = k_1^{(s)}\log\left(k_2^{(s)}\beta^{(s)}+1\right) \tag{23}$$

where $k_1^{(s)}$ and $k_2^{(s)}$ are material parameters to be determined experimentally. The integration of the static hardening variables evolution law provides the hardening energy:

$$\begin{aligned}\widetilde{\psi}^p(\boldsymbol{\beta}) &:= \sum_{s=1}^{6}\int_0^{\beta^{(s)}} \widetilde{\chi}^{(s)}\left(\bar{\beta}\right)\mathrm{d}\bar{\beta} \\ &= \sum_{s=1}^{6}\left\{\frac{k_1^{(s)}}{k_2^{(s)}}\left(k_2^{(s)}\beta^{(s)}+1\right)\left[\log\left(k_2^{(s)}\beta^{(s)}+1\right)-1\right]+1\right\}\end{aligned} \tag{24}$$

2.4.2. Brittle fracture

An AT1 form, where AT stands for Ambrosio and Tortorelli (1990), of the phase-field specific dissipation $w(d)$ in (13) is assumed, which implies that damage cannot develop until a critical value of the damage driving force has been achieved. Based on this assumption, the phase-field functions $\omega(d)$ and $w(d)$ are defined as

$$\omega(d) = (1-d)^2, \quad w(d) = \frac{3G_c}{8l_{0d}}\,d \tag{25}$$

where G_c is the material toughness and l_{0d} the phase-field internal length. The AT1 fracture diffusion coefficient c_d is defined as $c_d = {}^3\!/_4\, G_c\, l_{0d}$, and the viscous coefficient η_f in (11) as $\eta_f = \bar{\eta}\left(G_c/l_{0d}\right)$.

To avoid the promotion of crack propagation by predominantly compressive stress states, different ways to split the energy in the damage driving force have been proposed in the literature (see, e.g., Comi and Perego (2001), Amor et al. (2009) and Miehe et al. (2010)). In the current model, the entire energy $\hat{\widetilde{\psi}}$ will be considered in the fracturing process, while the damage activation criterion will be suitably modified to avoid damage growth under compression states (see Section 3.1).

3. Interaction between ductile and brittle dissipation mechanisms

In the variational elastoplastic-brittle-fracture model resulting from the stationarity of the functional $\mathcal{L}^n(S)$ in (11), the only coupling between the plastic and fracture dissipation mechanisms appears in the fracture driving force $\mathcal{G}$ in (18), through the energy term $\hat{\widetilde{\psi}}$, while the fracture dissipation $\mathcal{G}_c$ is the same as the one of the purely brittle case. As discussed in several works on ductile phase-field fracture (see, e.g., Ambati et al. (2015), Huang and Gao (2019), Yin and Kaliske (2020), Hu et al. (2021) and Marengo and Perego (2023b)), numerical tests have shown that this weak coupling is not flexible enough to accurately describe the wide spectrum of ductile–brittle behaviors exhibited by different materials. Inspired by what was proposed in Marengo and Perego (2023b), the approach to plasticity-driven phase-field fracture evolution in paperboard, proposed here, relies on the definition of a scalar function $f(\xi)$ of a suitable directional measure ξ of the plastic strains $\boldsymbol{\varepsilon}^p$, hereafter referred to as *modulation function*. Its purpose is to modulate the evolution of the critical fracture energy, based on the evolution of the plastic process zone. To this purpose, a new, non-variational interaction term is introduced in the expression of the critical energy release rate functional $\mathcal{G}_c$ (18b):

$$\begin{aligned}\mathcal{G}_c^p(\xi,d)[\delta d] := &\underbrace{\int_{\Omega_0} f(\xi)\,w'(d)\,\delta d\,\mathrm{d}\Omega_0}_{\textit{interaction term}} \\ &+ \underbrace{\int_{\Omega_0}\left\{\left[w'(d)+\frac{\eta_f}{\Delta t}\,\Delta d\right]\delta d + c_d\,\boldsymbol{\nabla} d\cdot\boldsymbol{\nabla}\delta d\right\}\mathrm{d}\Omega_0}_{\mathcal{G}_c(d)[\delta d]}\end{aligned} \tag{26}$$

where the superscript p of $\mathcal{G}_c^p$ underlines that the expression in (26) contains a new ductile–brittle interaction term. As it will be discussed in the next Section, the effect of the new interaction term is that damage, measured by the phase-field order parameter d, can only grow when the plastic process zone in a stress concentration region has fully developed, as measured by the directional plastic strain measure ξ.

As in Marengo and Perego (2023b), the definition of the modulation function $f(\xi)$ in (26) is obtained based on the study of the one-dimensional homogeneous case. However, while an isotropic material was considered in Marengo and Perego (2023b) and $\xi = \alpha$ was assumed for the definition of the plastic strain measure, α being the equivalent plastic strain, a different definition of ξ has to be considered in the present anisotropic context.

Following Marengo and Perego (2023b), the modulation function is chosen such that damage is zero until a critical value ξ_{cr} of the plastic strain measure ξ is achieved. Furthermore, to take into account the irreversible nature of the plastic dissipation process, the plastic measure ξ satisfies the condition $\Delta\xi \geq 0$ in the finite step during every evolution process. The following form of the modulation function $f(\xi)$, replicates the form proposed in Marengo and Perego (2023b), however now controlled by ξ, and satisfies the above conditions:

$$f+1 = \begin{cases}\dfrac{\widetilde{\mathcal{H}}}{\bar{g}} & \text{if} \quad \xi \leq \xi_{cr} \\ \left(1-\bar{d}\right)\dfrac{\widetilde{\mathcal{H}}}{\bar{g}} + \bar{d} & \text{if} \quad \xi_{cr} < \xi < \xi_{cr}+\Delta\xi_{cr} \\ 1 & \text{if} \quad \xi \geq \xi_{cr}+\Delta\xi_{cr}\end{cases} \tag{27}$$

with $\Delta\xi_{cr}$ defining the increment of $\xi > \xi_{cr}$ beyond which $f(\xi)$ achieves its minimum constant value $f_{min} = 0$, corresponding to the purely brittle portion of $\mathcal{G}_c^p$, in the sense specified before. The history function $\widetilde{\mathcal{H}}$ is defined as:

$$\widetilde{\mathcal{H}} := \mathcal{H} + \widetilde{\psi}^p + \Delta\widetilde{\phi}^p \tag{28}$$

while $\mathcal{H}$, inspired to the history variable introduced in Miehe et al. (2010), is taken to be:

$$\mathcal{H} = \max\left(\widetilde{\psi}^e, \mathcal{H}^n\right) \tag{29}$$

This last condition ensures that in the case of elastic unloading, i.e., $\widetilde{\psi}^e < \widetilde{\psi}^{e\,n}$, the modulation function cannot decrease, n being the time step number. Finally, the function $\bar{d}(\xi)$ in (27) has been defined in Marengo and Perego (2023b) ans is such that $\bar{d}=0$ for $\xi < \xi_{cr}+\Delta\xi_{cr}$ and $\bar{d}=1$ for $\xi \geq \xi_{cr}+\Delta\xi_{cr}$.

As discussed in Marengo and Perego (2023b), the interaction between the ductile and brittle dissipation mechanisms can be fully controlled by the two, easily identifiable parameters ξ_{cr} and $\Delta\xi_{cr}$. ξ_{cr} has the purpose to delay the onset of damage and, therefore, the beginning of the softening branch in the load–displacement curve, while $\Delta\xi_{cr}$ controls its slope (see Marengo and Perego (2023b) for a more detailed discussion on the role of these two parameters).

3.1. Plastic strain measure

In the case of an isotropic material with a single hardening mechanism and obeying von-Mises criterion, as in Marengo and Perego (2023b), the equivalent plastic strain $\alpha = \int_0^t \sqrt{2/3\,\dot{\boldsymbol{\epsilon}}^p : \dot{\boldsymbol{\epsilon}}^p}\,\mathrm{d}\tau$ plays the role of a scalar measure of the plastic deformation at a point. Then, it is enough to define a critical value α_{cr}, corresponding to the onset of damage and a second value $\Delta\alpha_{cr}$, such that for $\alpha \geq \alpha_{cr} + \Delta\alpha_{cr}$ continuing plasticity does not affect the critical energy release functional $\mathcal{G}_c^p$ in (26). In the isotropic case, the plastic strain measure ξ, appearing in the modulation function $f(\xi)$, can then be simply defined as $\xi^{iso} := \alpha/\alpha_{cr}$, with a critical value $\xi_{cr}^{iso} = 1$. For $\xi^{iso} < 1$ no damage occurs, while at $\xi^{iso} = 1$ damage starts to grow and for $\xi^{iso} \geq 1 + \Delta\xi_{cr}^{iso}$, with $\Delta\xi_{cr}^{iso} = \Delta\alpha_{cr}/\alpha_{cr}$, one has $\bar{d} = 1$, $f(\xi^{iso}) = 0$, and the fracture process is fully active.

In the case of anisotropic materials, the crucial point is to introduce a suitable measure ξ of the plastic deformation accounting for the fact that plastic strains in different anisotropic material directions must have a different effect on damage growth and therefore must be measured by ξ in a different way. To this purpose, a critical value is defined for each plastic strain component $(\epsilon_1^p,\ \epsilon_2^p,\ \gamma_{12}^p)$ in the material reference frame (i.e., for each material direction a different critical value is defined, $\epsilon_1^{cr},\ \epsilon_2^{cr},\ \gamma_{12}^{cr}$). Then, inspired by the expression of the yield criterion in the stress space (22), a directional criterion for the onset of damage is formulated in terms of the plastic strain components with respect to the material orthotropy axes, as follows:

$$\left(\frac{\langle\epsilon_1^p\rangle_+}{\epsilon_1^{cr}}\right)^{2k_p} + \left(\frac{\langle\epsilon_2^p\rangle_+}{\epsilon_2^{cr}}\right)^{2k_p} + \left(\frac{\left|\gamma_{12}^p\right|}{\gamma_{12}^{cr}}\right)^{2k_p} - 1 = 0 \tag{30}$$

where the exponent k_p controls the interaction between the different modes. The Macaulay brackets $\langle\cdot\rangle_+$ in the first two terms prevent damage growth in compression-dominated states, while only the absolute value of the shear strain plays a role. The presence of the Macaulay brackets $\langle\cdot\rangle_+$ avoids introducing a strain energy split, usually based on a different consideration of volumetric and deviatoric energy components or of positive and negative principal strains. Besides allowing for significant computational simplifications, the split in (30) also avoids the inconsistencies deriving from the combined adoption of an energy split together with an effective stress approach, as highlighted in Marengo and Perego (2023b).

As in the isotropic case, a scalar plastic strain measure ξ, providing the *distance* of the current plastic deformation state from the limit activation condition (30), is introduced. The activation criterion is then homothetically scaled by the factor ξ as follows:

$$\left(\frac{\langle\epsilon_1^p\rangle_+}{\xi\,\epsilon_1^{cr}}\right)^{2k_p} + \left(\frac{\langle\epsilon_2^p\rangle_+}{\xi\,\epsilon_2^{cr}}\right)^{2k_p} + \left(\frac{\left|\gamma_{12}^p\right|}{\xi\,\gamma_{12}^{cr}}\right)^{2k_p} - 1 = 0 \tag{31}$$

so that the critical condition in (30) is achieved when $\xi = \xi_{cr} = 1$. Eq. (31) can be solved with respect to ξ,

$$\xi(\boldsymbol{\epsilon}^p) = \left[\left(\frac{\langle\epsilon_1^p\rangle_+}{\epsilon_1^{cr}}\right)^{2k_p} + \left(\frac{\langle\epsilon_2^p\rangle_+}{\epsilon_2^{cr}}\right)^{2k_p} + \left(\frac{\left|\gamma_{12}^p\right|}{\gamma_{12}^{cr}}\right)^{2k_p}\right]^{1/2k_p} \tag{32}$$

providing the sought anisotropic measure of the distance from the critical state of damage activation. In Fig. 1, the homothetic surfaces at constant ξ are shown in the space of the scaled components of the plastic strain tensor, expressed in the reference frame of the anisotropic material directions. Scaled components mean that each plastic strain component is divided by its critical value. In this space, for the interaction exponent $k_p = 1$, for each constant value of ξ Eq. (31) defines one eighth of a sphere and (32) defines a radial distance.

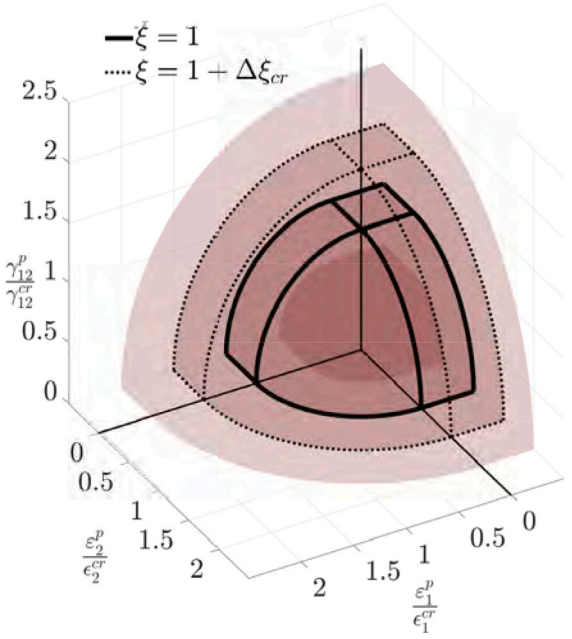

Fig. 1. Loci of constant plastic strain measure ξ in the in-plane plastic strain space (material reference frame), with $k_p = 1$ and $\Delta\xi_{cr} = 0.5$. The distance between two loci is $\Delta\xi = 0.5$. The solid line corresponds to the limit surface of damage activation (30), and the dashed line to the fracture onset criterion, $\xi = 1 + \Delta\xi_{cr}$.

The condition $\xi(\boldsymbol{\epsilon}^p) < 1$ in Fig. 1 denotes the undamaged state, while $\xi(\boldsymbol{\epsilon}^p) = 1$ (solid line) corresponds to the critical surface, i.e., to the onset of damage. Finally, for $\xi(\boldsymbol{\epsilon}^p) \geq 1 + \Delta\xi_{cr}$ the fracture process is fully active. A final important remark concerns the role of the Macaulay operator in the criterion (30). As already mentioned, the proposed model does not include any energy split to prevent the crack propagation in compressive-dominated states. Instead, the proposed plasticity-driven activation criterion (stated in the material reference frame) assumes that only the positive part of the normal plastic strain components can contribute to the crack evolution, while the shear component contributes independently of its sign. The new damage activation criterion (30) requires the calibration of five additional material parameters, i.e. ϵ_1^{cr}, ϵ_2^{cr}, γ_{12}^{cr}, the exponent k_p and $\Delta\xi_{cr}$.

It should be noted that when $\xi \geq \xi_{cr} + \Delta\xi_{cr}$, one has $f(\xi) = 0$, the effect of the modulation function vanishes, and the activation condition (20) holds, where G_c is used rather than G_c^p, as in (26). At this point, the original phase-field variationally consistent structure is recovered. This has the beneficial effect that the Γ-convergence property of the variational phase-field model is recovered in the final stage of material failure. On the other hand, one should also notice that only one value of the fracture energy is defined in this way, so that the energy needed to generate new fracture surfaces in this final stage is the same in all directions as for an isotropic material. This is a limitation of the model, which however has little impact since experimental evidence shows that MD and CD fracture energies are in general not so different (see, e.g. Alzweighi et al. (2023)) and the amount of fracture energy dissipated in the final phase, when $f(\xi) = 0$, is limited. It should also be noted that, for the considered ductile material, the dissipated anisotropic plastic energy is dominant with respect to the fracture energy. Since damage activation and propagation are controlled by the anisotropic plastic measure ξ, the material anisotropic response can be accurately reproduced by the proposed model, as it will be shown by the numerical simulation of experimental fracture tests on paperboard.

4. Implementation

4.1. Discretization

The discretized version of the 2D problem is obtained by modeling the unknown fields $\mathbf{u}$, d and their gradients $\boldsymbol{\varepsilon}$ (expressed in Voigt notation. The same symbol is used for tensor and Voigt quantities with abuse of notation) and $\boldsymbol{\nabla} d$ over each element e as follows:

$$\mathbf{u} = \mathbf{N}_{\mathrm{u}}\,\hat{\mathbf{u}}_e \quad , \quad d = \mathbf{N}_{\mathrm{d}}\,\hat{\mathbf{d}}_e \tag{33a}$$

$$\boldsymbol{\varepsilon} = \mathbf{B}_{\mathrm{u}}\,\hat{\mathbf{u}}_e \quad , \quad \boldsymbol{\nabla} d = \mathbf{B}_{\mathrm{d}}\,\hat{\mathbf{d}}_e \tag{33b}$$

where $\hat{\mathbf{u}}_e$ is the vector of nodal displacements, $\mathbf{N}_{\mathrm{u}}$ is the matrix of displacement shape functions, $\mathbf{B}_{\mathrm{u}}$ is the matrix of displacement compatibility, $\hat{\mathbf{d}}_e$ is the vector of nodal phase-field values and $\mathbf{B}_{\mathrm{d}}$ the matrix of the gradients of the phase-field shape functions. The global assembly is formally performed with the boolean connectivity matrices $\mathbf{C}_{e,\mathrm{u}}$, and $\mathbf{C}_{e,\mathrm{d}}$ such that:

$$\hat{\mathbf{u}}_e = \mathbf{C}_{e,\mathrm{u}}\,\hat{\mathbf{u}} \quad , \quad \hat{\mathbf{d}}_e = \mathbf{C}_{e,\mathrm{d}}\,\hat{\mathbf{d}} \tag{34}$$

and the symbols without the element subscript e denote assembled global vectors.

4.2. Balance equations

All the material quantities are expressed in the material reference frame where indices 1,2 refer to the MD and CD directions, respectively. In Voigt notation, the in-plane effective stress and strain vectors are $\widetilde{\boldsymbol{\sigma}} = (\widetilde{\sigma}_1, \widetilde{\sigma}_2, \widetilde{\tau}_{12})^{\mathrm{T}}$ and $\boldsymbol{\varepsilon} = (\varepsilon_1, \varepsilon_2, \gamma_{12})^{\mathrm{T}}$. The linear elastic law is written as $\widetilde{\boldsymbol{\sigma}} = \widetilde{\mathbf{D}}(\boldsymbol{\varepsilon} - \boldsymbol{\varepsilon}^p)$, where the matrix of effective elastic moduli, expressed in the material frame, reads

$$\widetilde{\mathbf{D}} = \frac{1}{1 - \nu_{12}\nu_{21}} \begin{bmatrix} E_1 & \nu_{21} E_1 & 0 \\ \nu_{12} E_2 & E_2 & 0 \\ 0 & 0 & G_{12}\left(1 - \nu_{12}\nu_{21}\right) \end{bmatrix} \tag{35}$$

where E_1 and E_2 are the elastic moduli in the material directions, ν_{12} and ν_{21} are the Poisson ratios and G_{12} the in-plane shear modulus. In the Xia's yield function (22), the normal stress $\sigma_n^{(s)}$ is obtained from $\sigma_n^{(s)}(\widetilde{\boldsymbol{\sigma}}) = \mathbb{m}^{(s)\mathrm{T}}\widetilde{\boldsymbol{\sigma}}$, where $\mathbb{m}^{(s)} = [(n_1^{(s)})^2, (n_2^{(s)})^2, 2n_1^{(s)}n_2^{(s)}]^{\mathrm{T}}$ and $n_i^{(s)}$ are the components of the unit normal $\mathbf{n}^{(s)}$ to the sth mechanism in the stress space. The components of each normal are material parameters to be determined experimentally (Borgqvist et al., 2015), or using analytical relations (Borgqvist et al., 2014). The components always refer to the material reference frame.

The weak form of the equilibrium equation (14) and the complementarity equations in the fracture activation criterion $(19)_3$ are spatially discretized as follows:

$$\delta\hat{\mathbf{u}}^{\mathrm{T}} \left[\sum_{e=1}^{n_{el}} \mathbf{C}_{e,\mathrm{u}}^{\mathrm{T}} \left(\int_{\Omega_e} \mathbf{B}_{\mathrm{u}}^{\mathrm{T}}\, \omega\widetilde{\boldsymbol{\sigma}}\, \mathrm{d}\Omega_e - \int_{\Omega_e} \mathbf{N}_{\mathrm{u}}^{\mathrm{T}}\,\mathbf{b}\,\mathrm{d}\Omega_e - \int_{\partial\Omega_e} \mathbf{N}_{\mathrm{u}}^{\mathrm{T}}\,\mathbf{t}\,\mathrm{d}\Gamma_e \right) \right] = 0 \tag{36}$$

$$\Delta\hat{\mathbf{d}}^{\mathrm{T}} \left[\sum_{e=1}^{n_{el}} \mathbf{C}_{e,\mathrm{d}}^{\mathrm{T}} \left(\int_{\Omega_e} \left\{ \mathbf{N}_{\mathrm{d}}^{\mathrm{T}} \left[\omega' \,\hat{\widetilde{\psi}} + (f+1)\, w' + \frac{\eta_f}{\Delta t}\,\Delta d \right] + c_d\, \mathbf{B}_{\mathrm{d}}^{\mathrm{T}}\,\boldsymbol{\nabla} d \right\} \times \mathrm{d}\Omega_e \right) \right] = 0 \tag{37}$$

The element integrals are evaluated over the element nominal volume Ω_e. The element internal force vector $\mathbf{F}_{\mathrm{I},e}$, the external force vector $\mathbf{F}_{\mathrm{E},e}$, and the fracture activation vector $\mathbf{f}_{\mathrm{D},e}$ are defined as:

$$\mathbf{F}_{\mathrm{I},e} := \int_{\Omega_e} \mathbf{B}_{\mathrm{u}}^{\mathrm{T}}\, \omega\, \widetilde{\boldsymbol{\sigma}}\, \mathrm{d}\Omega_e \tag{38a}$$

$$\mathbf{F}_{\mathrm{E},e} := \int_{\Omega_e} \mathbf{N}_{\mathrm{u}}^{\mathrm{T}}\,\mathbf{b}\,\mathrm{d}\Omega_e + \int_{\partial\Omega_e} \mathbf{N}_{\mathrm{u}}^{\mathrm{T}}\,\mathbf{t}\,\mathrm{d}\Gamma_e \tag{38b}$$

$$\mathbf{f}_{\mathrm{D},e} := -\int_{\Omega_e} \left\{ \mathbf{N}_{\mathrm{d}}^{\mathrm{T}} \left[\omega' \,\hat{\widetilde{\psi}} + (f+1)\, w' + \frac{\eta_f}{\Delta t}\,\Delta d \right] + c_d\, \mathbf{B}_{\mathrm{d}}^{\mathrm{T}}\,\boldsymbol{\nabla} d \right\} \mathrm{d}\Omega_e \tag{38c}$$

The spatial discretization of the governing equations can be written as

$$\mathbf{F}_{\mathrm{I}} - \mathbf{F}_{\mathrm{E}} = \mathbf{0} \tag{39a}$$

$$\Delta\hat{\mathbf{d}} \geq \mathbf{0} \quad , \quad \mathbf{f}_{\mathrm{D}} \leq \mathbf{0} \quad , \quad \Delta\hat{\mathbf{d}}^{\mathrm{T}}\,\mathbf{f}_{\mathrm{D}} = 0 \tag{39b}$$

The internal force vector $\mathbf{F}_{\mathrm{I}}$ incorporates the nonlinear elastoplastic stress–strain dependence governed by the local complementarity problem (16), to be solved locally at each Gauss integration point. Since the elastoplastic law (16) is expressed in terms of effective quantities $\widetilde{\boldsymbol{\sigma}}, \widetilde{\boldsymbol{\chi}}$, damage does not enter into the solution of the elastoplastic problem and the classical return mapping algorithms and consistent tangent matrices can be used.

4.3. Staggered scheme

The set of governing equations (39) is solved by means of the alternate minimization scheme illustrated in Algorithm 1. At each time step from t^n to t^{n+1}, the input is the nodal solution $(\hat{\mathbf{u}}, \hat{\mathbf{d}})^n$ and the plastic strains and state variables $(\boldsymbol{\varepsilon}^p, \boldsymbol{\beta})^n$ at Gauss points at the end of the previous step, the new increment of displacement Dirichlet boundary conditions $\Delta\hat{\mathbf{u}}_{\mathrm{D}}$ and the increment of external forces $\Delta\mathbf{F}_{\mathrm{E}}$. The staggered scheme is solved with an iterative procedure, where i denotes the staggered iteration counter. First, the elastoplastic problem (39a) is solved for fixed phase-field $\Delta\hat{\mathbf{d}}_{i-1}$. Then, the equilibrium solution $\hat{\mathbf{u}}_k$ is used to solve the phase-field problem for frozen displacements and plastic strains. Finally, the residual $\mathtt{res}_{STAG}$ of the staggered scheme is computed. It measures again the nodal out-of-balance forces, but with the updated damage. The complementarity problem (39b) is solved using the Mangasarian (1977) Projected Successive Over-Relaxation algorithm (PSOR), following the approach proposed in Marengo et al. (2021).

5. Numerical simulations

The model capabilities are assessed by comparing the results of numerical simulations and experimental tests carried out in climate controlled laboratory (see Section 5.2). The simulations are performed assuming plane stress conditions and using linear triangular elements with a single integration point, except for the first example, where a single quadrilateral element with four Gauss points is used. The considered paperboard thickness is $t = 0.41$ mm. The elastic parameters and the exponent k of Xia's yield function (22) are reported in Table 1.

The six in-plane yield mechanisms have already been discussed in Section 2.4. The adopted values of initial yield stresses $\bar{\sigma}_y^{(s)}$, hardening parameters k_1, k_2 (see (23)) and a description of each mechanism are listed in Table 2. Hardening is assumed to occur only in tension and shear, while the same material properties are used for positive and negative shear.

The brittle fracture material properties are the toughness $G_c = 6\,\mathrm{N/mm}$ and the internal length scale parameter $l_{0d} = 2$ mm (see, e.g., Niskanen et al. (2001)). The viscous coefficient is $\bar{\eta} = 10^{-2}\ \mathrm{s}^{-1}$. The simulations are carried out under tensile loading conditions for different relative orientations θ between the material direction CD and the load direction. The material layouts that have been tested are tension along the CD direction, i.e. $\theta = 0°$, tension along the MD direction, i.e. $\theta = 90°$, and some intermediate directions $\theta = 22.5°, 45°, 67.5°$. The ductile fracture parameters for paperboard are listed in Table 3.

Algorithm 1: Minimization scheme

input $(\hat{\mathbf{u}}, \hat{\mathbf{d}})^n$, $(\boldsymbol{\varepsilon}^p, \boldsymbol{\beta})^n$, $\Delta\hat{\mathbf{u}}_{\mathrm{D}}$, $\Delta\mathbf{F}_{\mathrm{E}}$
initialize $(\hat{\mathbf{u}}, \hat{\mathbf{d}})_i = (\hat{\mathbf{u}}, \hat{\mathbf{d}})^n$
while ($res_{STAG} > TOL_{STAG}$) **do**
  update $i = i + 1$
  solve $\mathbf{F}_{\mathrm{I}}(\Delta\hat{\mathbf{u}}, \Delta\hat{\mathbf{d}}_{i-1}) - \mathbf{F}_{\mathrm{E}} = \mathbf{0} \quad \rightarrow \Delta\hat{\mathbf{u}}_i$
  solve $\Delta\hat{\mathbf{d}} \geq \mathbf{0} \quad , \quad \mathbf{f}_{\mathrm{D}}(\Delta\hat{\mathbf{u}}_i, \Delta\hat{\mathbf{d}}) \leq \mathbf{0} \quad , \quad \Delta\hat{\mathbf{d}}^{\mathrm{T}}\mathbf{f}_{\mathrm{D}}(\Delta\hat{\mathbf{u}}_i, \Delta\hat{\mathbf{d}}) = 0 \quad \rightarrow \Delta\hat{\mathbf{d}}_i$
  assemble $\mathbf{R}_{\mathrm{u}} = \mathbf{F}_{\mathrm{I}}(\Delta\hat{\mathbf{u}}_i, \Delta\hat{\mathbf{d}}_i) - \mathbf{F}_{\mathrm{E}}$
  compute $\mathrm{res}_{STAG} = \mathbf{R}_{\mathrm{u}}^{\mathrm{T}}\mathbf{R}_{\mathrm{u}}$
end
output $(\hat{\mathbf{u}}, \hat{\mathbf{d}})^n = (\hat{\mathbf{u}}, \hat{\mathbf{d}})_i$, $(\boldsymbol{\varepsilon}^p, \boldsymbol{\beta})^n = (\boldsymbol{\varepsilon}^p, \boldsymbol{\beta})_i$

Table 1
Elastoplastic material properties.

E_1	E_2	ν_{12}	G_{12}	k
5.310	2.203	0.396	1.370	3
GPa	GPa	–	GPa	–

Table 2
Yield limit and hardening parameters of each yield mechanism.

Yield mechanism	Description	$\bar{\sigma}_y$	k_1	k_2
1	Tension MD	15.00	12.00	300.00
2	Tension CD	8.00	4.50	230.00
3	Positive shear	5.00	6.00	150.00
4	Compression MD	22.06	–	–
5	Compression CD	16.70	–	–
6	Negative shear	5.00	6.00	150.00
		GPa	–	–

Table 3
Ductile fracture parameters for tested paperboard material.

ϵ_1^{cr}	ϵ_2^{cr}	γ_{12}^{cr}	k_p	$\Delta\xi_{cr}$
0.035	0.087	0.11	0.75	0.2

5.1. Single element

A single element is used to highlight the main features of the modulation function. The geometry of the element square shape of size $L = 1$ mm, the boundary conditions and material orientation θ are shown in Fig. 2. Specifically, θ represents the orientation between the vertical load direction and the CD direction (axis 2 in Fig. 2) or, alternatively, the angle between the horizontal direction and the MD direction (axis 1 in Fig. 2). A constant vertical displacement increment $\Delta u = 0.001$ mm is imposed at each step, with a total number of steps $n_{step} = 200$. For this test only, the viscous coefficient is $\bar{\eta} = 0$ s^{-1}. The material properties of paperboard listed in Tables 1–3 have been used also for this single element test. For the boundary conditions prescribed in Fig. 2, the stress and strain fields are uniform in the element (i.e., the response is the same at the four Gauss points).

The engineering strain is computed as $\varepsilon = u/L$. The reaction force R is measured at the top nodes in the vertical direction. The engineering stress is then $\sigma = R/(L\,t)$, where the thickness t is defined at the beginning of this Section. In Fig. 3(a), the plot of the engineering stress versus strain is shown for the different orientations θ. In all layouts, as long as the plastic deformation measure is $\xi < 1$, the response is purely elastoplastic without damage, confirming the correct effect of the modulation function $f(\xi)$ in modulating the competition between the plastic and fracture dissipation mechanisms.

In the subsequent figures, the evolution of the modulation function f, of the fictitious phase-field history $\bar{d}$, and of the plastic strains $\boldsymbol{\varepsilon}^p$ are shown in the material plastic strain space for one of the four Gauss points of the element in Fig. 2. The modulation function and fictitious phase-field history are depicted versus the plastic strain measure ξ in Fig. 3(b). The evolution of $\bar{d}$ is the same for all material orientations since it is defined as a function of ξ only, whereas the modulation function changes with the orientation. From these curves, the effect of the definition of f given in (27) can be appreciated. f is defined as the product of a user-defined part $(1 - \bar{d})$ and of a problem-dependent part $\widetilde{\mathcal{H}}/\bar{g}$, which is defined by the problem response, depending on geometry, boundary conditions, and material orientation. This second contribution is responsible for the different f curves in Fig. 3(b). However, all f curves share the same peak at $\xi = 1$ and minimum value $f = 0$ at $\xi = 1 + \Delta\xi_{cr} = 1.5$. The fact that the MD and CD curves lie below those of the other orientations is justified by the fact that several plastic mechanisms are activated for the intermediate layouts. This leads to a higher value of the term $\widetilde{\mathcal{H}}/\bar{g}$. In Fig. 3(c), the element deformed shapes for different material orientations are represented with a four-times amplification factor of displacements.

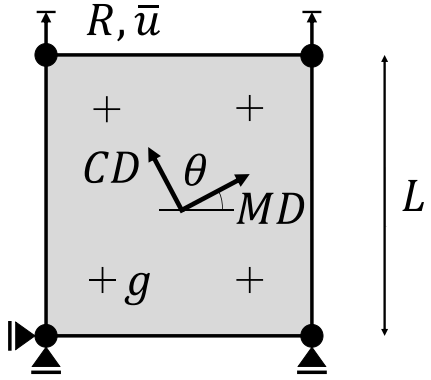

Fig. 2. Single quadrilateral element geometry, boundary conditions and material orientation θ.

The damage activation criterion defined in (30) with $k_p = 1$ is shown in Fig. 3(d) in the material plastic strain space $\left(\varepsilon_1^p, \varepsilon_2^p, \gamma_{12}^2\right)$. The colored lines departing from the origin describe the evolution of the plastic strain components $\left(\langle\varepsilon_1^p\rangle_+, \langle\varepsilon_2^p\rangle_+, \left|\gamma_{12}^p\right|\right)$ for different orientations. The solid black line denotes the intersection of the surface $\xi = 1$, corresponding to the damage activation condition, with the three planes $\varepsilon_1^p = 0, \varepsilon_2^p = 0, \gamma_{12}^p = 0$. As in Fig. 3(b), the dashed line corresponds to the surface $\xi = 1.5$ (i.e., when $\bar{d} = 1$) intersecting the same planes.

5.2. Experimental setup

Experimental tensile tests on paperboard strips have been carried out in a climate controlled laboratory with conditions in compliance with ISO 187 guidelines, with a humidity range of 50% ± 2% and a

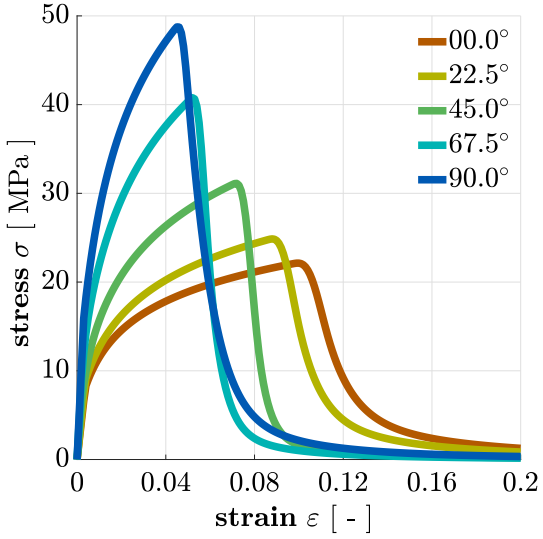

(a) Engineering stress vs. strain

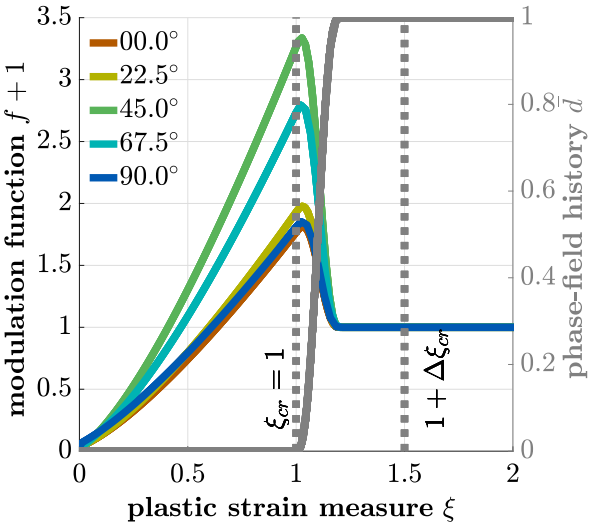

(b) Modulation function and fictitious phase-field evolution

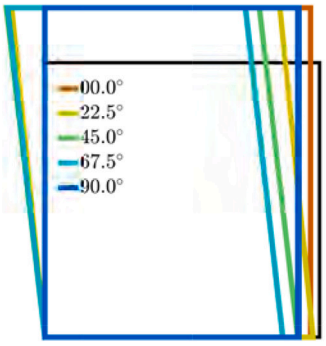

(c) Element deformed shapes for different layouts θ at final step $u = 1\,mm$. Black lines denote undeformed shape.

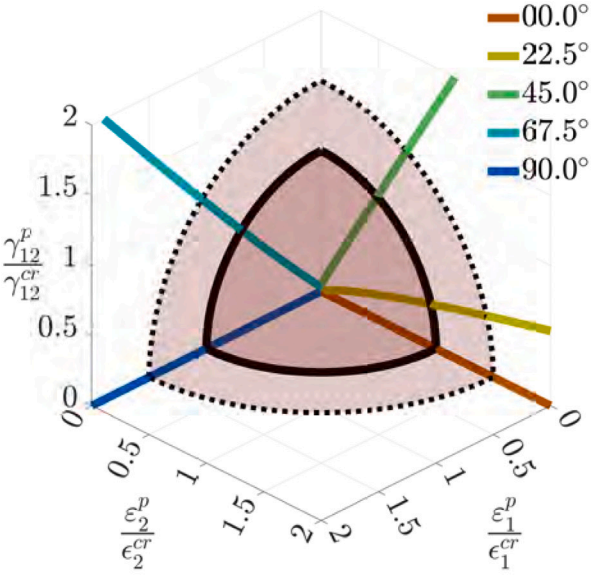

(d) Activation criterion in plastic strain space (material frame). The solid line corresponds to $\xi = 1$, the dashed line to $\xi = 1 + \Delta\xi_{cr}$, where $\Delta\xi_{cr} = 0.5$. An exponent $k_p = 1$ is assumed in (31).

Fig. 3. Single quadrilateral element. Element response for different material orientations.

temperature range of 23 °C ± 1 °C. For all experimental investigations, use is made of a single-ply, bleached, and clay-coated paperboard with a nominal basis weight of 315 g/m^2. Paperboard strips of two different lengths and with different orientations with respect to the loading direction have been tested to calibrate the model parameters (Section 5.3). The number of tested specimens for each material orientation is 3 (CD), 9 (22.5°), 8 (45°), 11 (67.5°), and 9 (MD) for the short span specimens, while it is 2 (CD), 5 (22.5°), 6 (45°), 5 (67.5°) and 5 (MD) for the long span specimens. Several tests in CD direction have been carried out also on specimens with width different from the reference. Since no significant difference (i.e., within the standard scatter observed for the tests on specimens of the reference width and also for other tests on material belonging to the same batch, see Alzweighi et al. (2023) where 2.14% (long-span) and 3.85% (short-span) standard deviation with respect to the mean value was obtained) related to the width has been observed, no other tests have been conducted in CD, and only the 2 tests in CD on the long-span specimens of the reference width have been used for the numerical simulations.

Then, strips containing a central circular hole, again of two different lengths and with different orientations regarding the loading direction, have been tested using the same material parameters previously identified to assess the model predictive capability (Section 5.4). In this latter case, the number of tested specimens is 5 for each of the three tested material orientations (MD, 45°, and CD) for both short and long span specimens.

Material parameters in (22) defining the plastic behavior have been taken from the literature and manually refined to reproduce the experimental tests accurately. Limit values of plastic strain components ϵ_1^{cr},

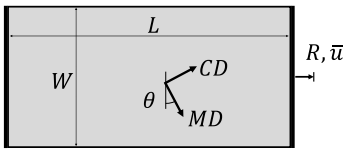

Fig. 4. Tensile test on paperboard strip. Geometry, boundary conditions and material orientation θ.

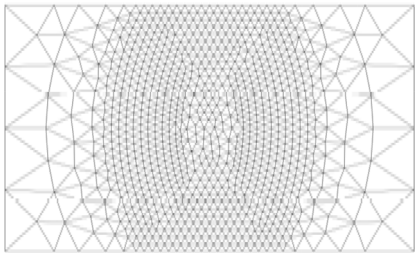

Fig. 5. Tensile test on paperboard strip. Short-span strip mesh (horizontal loading direction).

ϵ_2^{cr} in (30) have been obtained from uniaxial tests in material anisotropy directions based on the specimens peak response. ϵ_{12}^{cr} has been defined using the same technique described in Xia et al. (2002) and Borgqvist et al. (2014) for the definition of the yield surface. Due to lack of experimental data the exponent is taken as $k_p = 1$. The fracture energy G_c has been defined based on literature values for the considered type of paperboard.

The boundary conditions enforced by the clamps in the experimental setup constrain the displacement field in all directions. The bottom constraint works as a fixed clamp, while the top one prevents all horizontal displacements and enforces a vertical displacement. The specimen length L, to be defined in Sections 5.3 and 5.4, measures the distance between the two constraints. In the experimental campaign, all specimens failed far from the clamps and have therefore been considered reliable. This condition of rupture far from the clamps is rather difficult to obtain in the numerical simulations, since there is no information on possible material heterogeneity and thickness variability, which are, therefore, not accounted for in the numerical model. Hence, to avoid specimen failure near the clamps, for the short strip case, where the influence of the constraints is more significant, the finite elements in a small central region 2 mm high have been weakened by 20% in terms of initial yield stresses $\bar{\sigma}_y^{(s)}$ and material toughness. This does not significantly affect the global response in terms of reaction force, yet it drastically changes the crack location and pattern that otherwise might not resemble the experimental evidence.

5.3. Tensile test on paperboard strip

The model is used first to simulate the tests on paperboard strips without the hole, of two different lengths and varying material orientation with respect to the loading direction. The geometry, boundary conditions, and material orientation θ are shown in Fig. 4. The specimens have a rectangular shape with width $W = 15$ mm and two lengths $L = 25$ and 90 mm. The specimens with $L = 25$ mm are called *short-span*, while the specimens with $L = 90$ mm are called *long-span*. The paperboard strip is fully clamped on one of the short sides, while on the opposite side, a clamp enforces a displacement along the longitudinal direction. In the numerical simulations, a non-uniform increment of the Dirichlet boundary conditions Δu is applied at each time step, with smaller increments used during the damage localization phase.

The material properties defining the anisotropic plastic model are shown in Table 3 for Material II. These parameters have been calibrated to match the response of both the short and long-span strips. The minimum element size is $h_e = 0.5$ mm, and the resolution of the phase-field internal length is $l_{0d}/h_e = 4$.

The mesh for the short-span specimen is shown in Fig. 5. The same mesh has been used in the localization zone of the domain also for the long-span specimen, while the element size remains coarser outside this region. For both the short and long-span tests, the initial yield stresses $\bar{\sigma}_y^{(s)}$ and the material toughness G_c have been reduced to promote damage onset and crack formation in the central part of the specimen. Otherwise, a systematic failure near the clamps would occur. In Fig. 6, the reaction force R in the same direction as the enforced displacement u is shown for the different material layouts θ and both specimens families. The simulation results (thick lines) are shown together with the experimental results (thin lines). For the experimental curves, only the maximum and minimum envelopes of experimental points are depicted.

The simulations show the model capability, thanks to the modulation function $f(\xi)$, to properly capture the initiation of the damage process with subsequent crack propagation, and the orthotropic material response for varying orientation, thanks to the anisotropic plastic strain measure ξ and to the used activation criterion (30). Furthermore, the results in Fig. 6a and b, obtained with the same set of parameters, show that the size-effect is well described, with notable embrittlement of the softening response for the long-span specimen. However, it should be noted that the curves for the 22.5°, 45°, and 67.5° short specimens exhibit a final stage of the softening curve that is significantly more brittle than the corresponding experimental enclosing (the curves for the 0° and 90° short specimen are instead acceptably accurate also in this range). This may be due to the fact that in the final part of the test, the modulation function vanishes, and the fracture energy becomes isotropic, i.e., it does not change with the material orientation. It is also possible that the discrepancy be due to other dissipation mechanisms, activated only in the final stage of paper rupture, such as frictional sliding between fibers, that are not included in the model and therefore cannot be reproduced.

The comparison in terms of crack patterns between numerical simulations and experimental tests is shown in Fig. 7 for the short-span case and in Fig. 8 for the long-span one. The finite elements with $d \geq 0.95$ are plotted in white to render a realistic view of the crack pattern. While the force–displacement curves are generally accurately reproduced, it should be noted that the numerical crack patterns are qualitatively correct for the 0° and 90° material orientations, whereas they do not reproduce well the corresponding experimental path in the other cases, especially for the short-span case, showing a limited sensitivity to the material orientation with respect to the loading direction. This may be due to a limitation of the model that does not incorporate variations of the fracture energy with material orientation, or to the artificial initial weakening introduced in a thin central region of all numerical models with the purpose of promoting crack propagation far from the clamps. It should also be considered that the crack patterns in specimens of the same type exhibit a large scattering (see, e.g., the comparison in Fig. 9 of the crack pattern in two long-span specimens with 45° material orientation with respect to the loading direction), probably dependent on the intrinsic heterogeneity of the paperboard strip and/or other possible imperfections, such as an irregular strip thickness, which may induce a failure mode as the one in the $\theta = 67.5°$ case in Fig. 7(b), where the fracture plane is not orthogonal to the plane of the strip. The experimental results shown in Figs. 7(b) and 8(b) are therefore only indicative, since other specimens of the same type and orientations showed a significantly different crack path.

5.4. Tensile test on paperboard holed strip

The tensile strip tests in Section 5.3 have been used to calibrate the material parameters. The subsequent step is to assess the model predictability on a more complex boundary value problem, using the

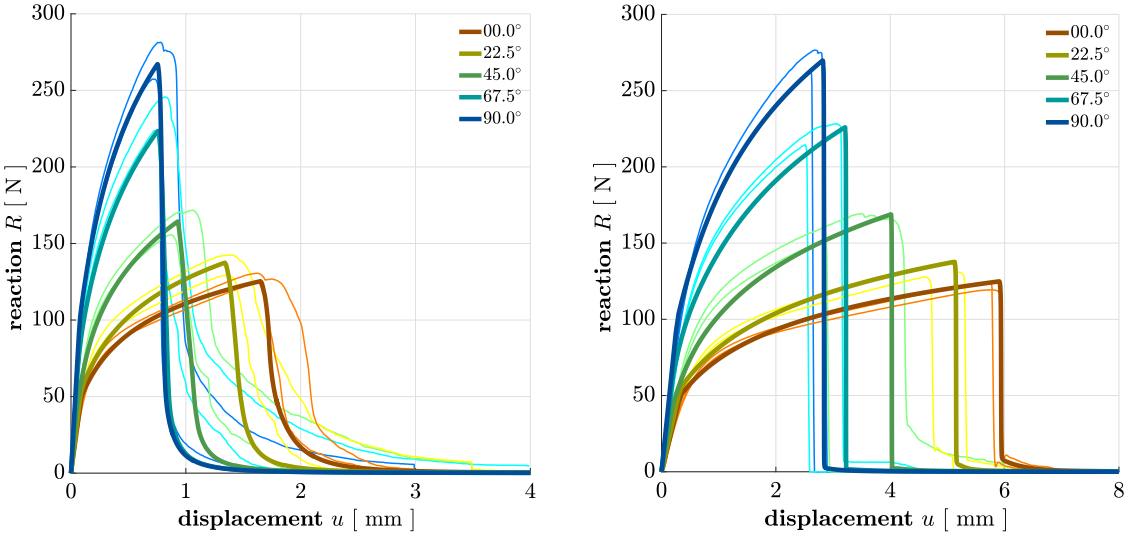

(a) Short span strip

(b) Long span strip

Fig. 6. Tensile test on paperboard strip. Reaction vs. displacement curves. Experimental tests envelopes (thin lines) and numerical results (thick lines).

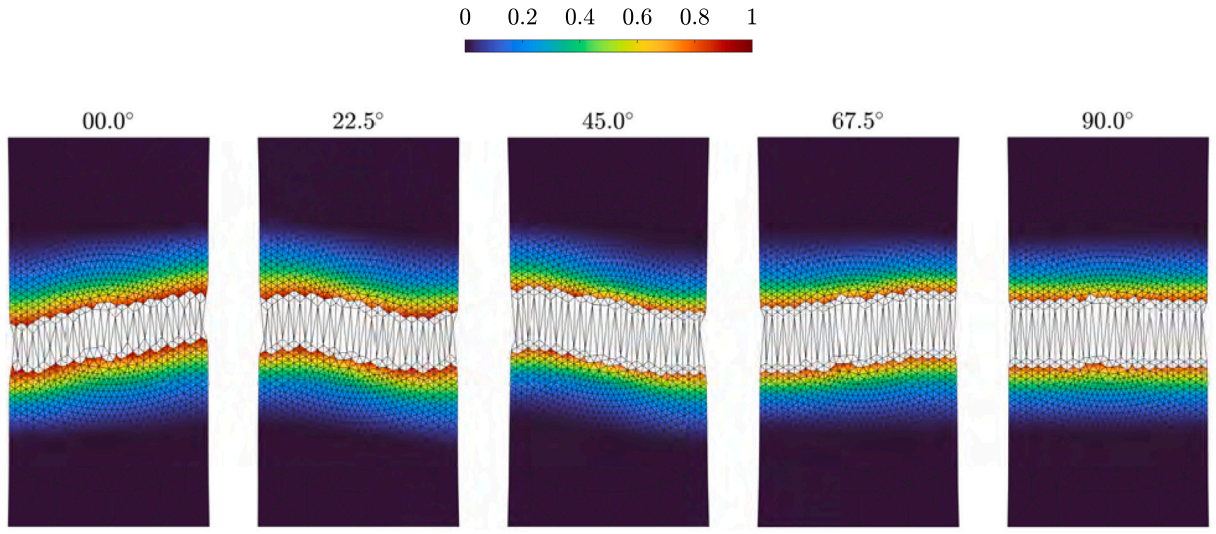

(a) Simulation

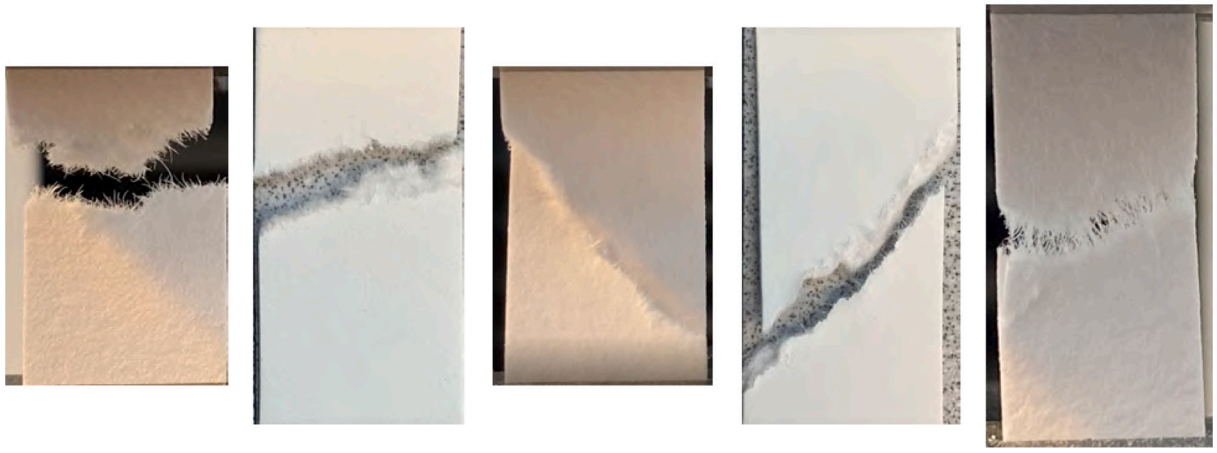

(b) Experimental

Fig. 7. Tensile test on paperboard strip. Short-strip. Phase-field profile and experimental specimens at failure. Finite elements with $d \geq 0.95$ are shown in white.

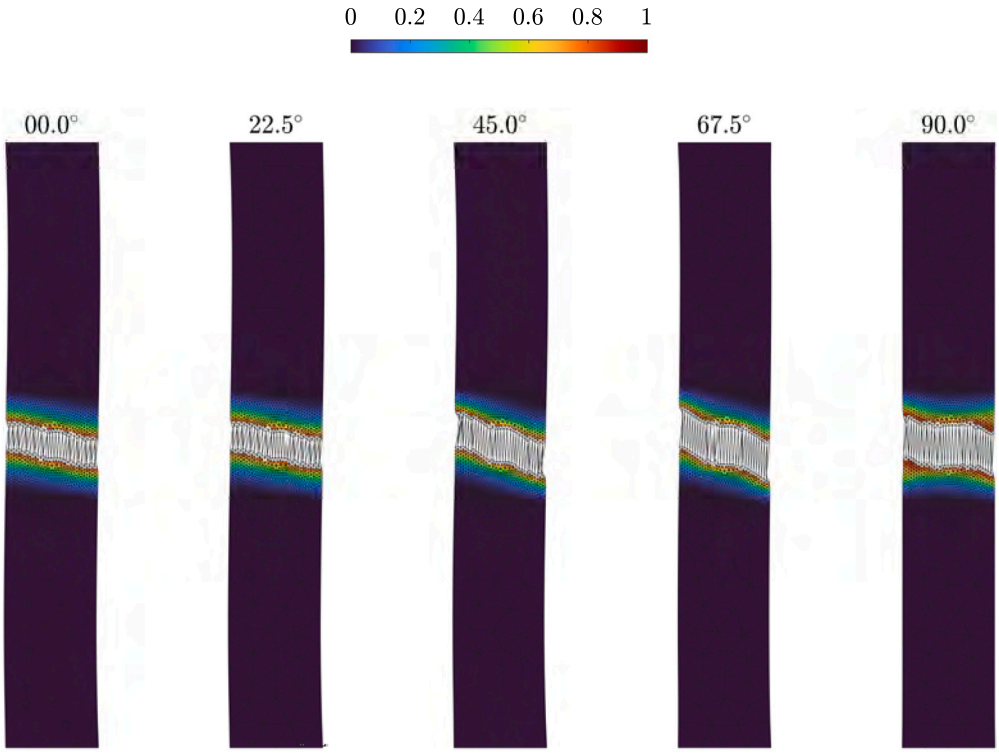

(a) Simulation

(b) Experimental

Fig. 8. Tensile test on paperboard strip. Long-strip. Phase-field profile and experimental specimens at failure. Finite elements with $d \geq 0.95$ are shown in white.

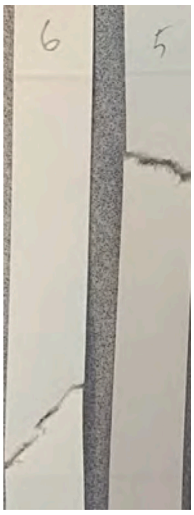

Fig. 9. Tensile test on long-span paperboard strip. Comparison of crack patterns between two specimens with 45° material orientation with respect to loading direction.

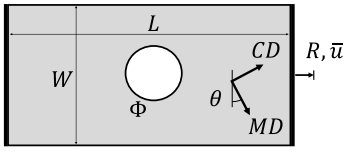

Fig. 10. Tensile test on paperboard holed strip. Geometry, boundary conditions and material orientation θ.

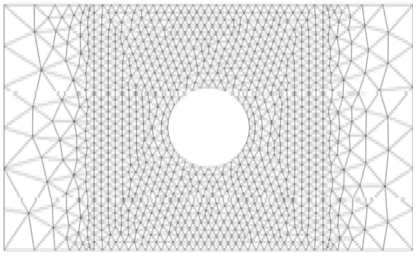

Fig. 11. Tensile test on paperboard holed strip. Short-span holed strip mesh (horizontal loading direction).

same set of parameters for material specimens of paperboard from the same material batch. The holed strip geometry, boundary conditions, and material orientation θ are shown in Fig. 10. The tests are restricted to the material orientations $\theta = 0°, 45°, 90°$. The specimen has a rectangular shape with fixed width $W = 15$ mm and two lengths $L = 25$ and 90 mm, with a central hole of diameter $\Phi = 5$ mm. The boundary conditions and the load steps are the same as those used for the strip without hole.

In this case, the material plastic properties are those in Table 3 for Material II. The minimum element size is $h_e = 0.5$ mm, and the resolution of the phase-field internal length is $l_{0d}/h_e = 4$.

The mesh for the short-span specimen is shown in Fig. 11. The same mesh has been used in the localization zone also for the long-span specimen, while the element size remains coarser outside this region. The reaction force R in the same direction as the enforced displacement u is shown in Fig. 12 for the different material layouts θ and for both the short and long-span specimens. The numerical results (thick lines) are reported with the experimental results (thin lines). For the experimental curves, only the maximum and minimum envelopes of experimental points are shown.

The curves in Fig. 9 confirm the good predictive capabilities of the model, with a realistic reproduction of the size effect. Good accuracy in terms of peak reaction and displacement values is obtained for the non-holed specimens and the holed long-span specimens. In the holed short-span case, while the peak reaction force is predicted with good accuracy for all material directions, the prediction in terms of displacement at peak reaction force underestimates the experimental results. In this case, the effects of the constraints do not decay sufficiently since the clamps are close to the hole edges. These effects are visible already in the elastoplastic pre-peak regime. The effects of the specimen size and the clamps in the case of short-span specimens have been discussed, e.g., in Hagman and Nygårds (2012) and Hägglund et al. (2004).

The numerical and experimental crack patterns are shown in Fig. 13 for the short-span case and in Fig. 14 for the long-span one. The comments relative to the non-holed specimens, at the end of the previous Subsection, also apply to the holed specimens, evidencing a limited sensitivity of the numerical crack direction to changes in material orientation.

6. Conclusions

A variational formulation of 2D small strain ductile fracture in orthotropic materials has been presented, with application to paperboard. The main features of the proposed model can be summarized as follows.

- A mixed, finite-step variational statement of small strain ductile fracture, with local plasticity and nonlocal phase-field has been presented, inspired by the work in Marengo and Perego (2023b) for small strain gradient plasticity with phase-field fracture. The variational statement applies to a rather general class of associative elastoplastic material models with damage, obeying the maximum dissipation principle, leading to a thermodynamically consistent set of constitutive relations. The resulting framework allows for elastoplastic models with multiple yield mechanisms and internal variables and can be conveniently adapted to model orthotropic materials.
- As in Marengo and Perego (2023b), the effective stress has been used in the yield function to ensure that yielding occurs only in the effective part of the damaged volume. Consequently, plasticity continues to develop until the final stage of material failure. Besides the physical motivations behind this choice, the use of an effective stress approach simplifies the implementation of the orthotropic elastoplastic model and the computation of its consistent tangent matrix. An AT1 brittle fracture dissipation approach has been adopted to guarantee the existence of a purely elastoplastic response before the onset of damage. Irreversibility of the phase-field dissipation has been rigorously enforced by solving the global linear complementarity problem associated with the fracture activation criterion through the explicit Projected Successive Over-Relaxation (PSOR) algorithm (Mangasarian, 1977), as proposed in Comi and Perego (1996) and Marengo et al. (2021). The elastoplastic in-plane behavior has been modeled according to Xia's orthotropic multi-surface yield criterion (Xia et al., 2002).
- Following recent publications, (e.g., Huang and Gao (2019), Yin and Kaliske (2020), Hu et al. (2021) and Marengo and Perego (2023b)), the variationally consistent plasticity-driven damage activation criterion has been modified into a non-variational form by introducing an additional term containing a modulation function. This function mediates the interaction and competition between plastic and brittle dissipation mechanisms. For the orthotropic material under consideration, the modulation function depends on a suitable directional measure of the plastic deformation. Different limit values of plastic strains in different material directions are defined and a corresponding plasticity-driven damage activation criterion is implemented. As a result, the variability in material toughness across distinct material directions is captured without considering additional damage fields or introducing a structural tensor in the gradient phase-field term.

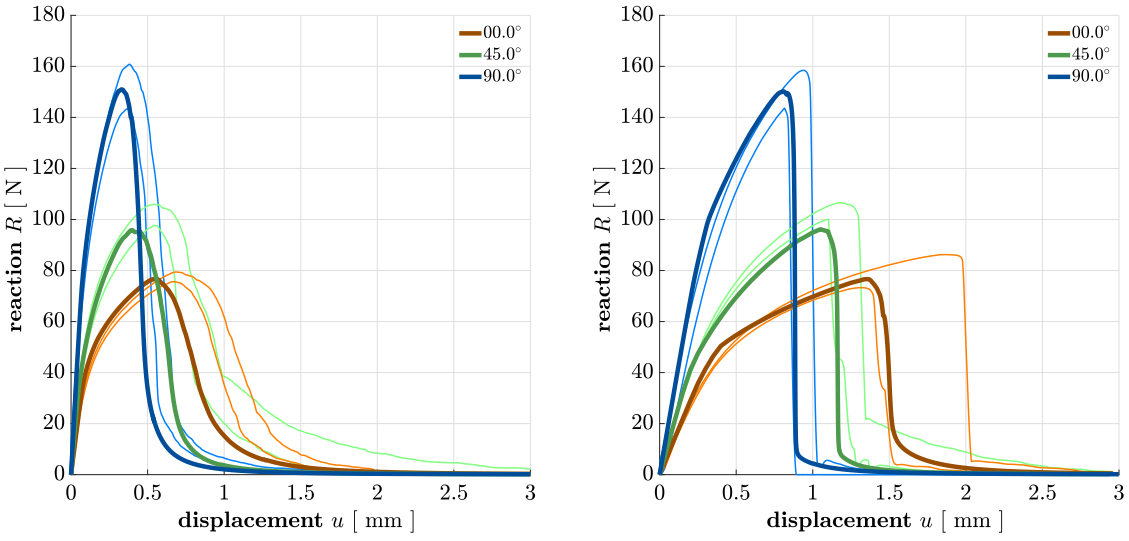

(a) Short span holed strip

(b) Long span strip

Fig. 12. Tensile test on paperboard holed strip. Reactions vs. displacements. Experimental tests envelopes (thin lines) and numerical results (thick lines).

- The introduction in the variational statement of the term containing the modulation function makes the formulation non-variational. However, the modulation function vanishes when the anisotropic plastic strain measure reaches the limit value $\xi \geq \xi_{cr} + \Delta\xi_{cr}$. At this point, the variational structure of the problem is recovered along with its Γ-convergence property.
- Rather than introducing a split of the released energy in the damage driving force, crack propagation under prevailing compression stress states has been prevented by considering only positive normal plastic strain components in the plasticity-driven damage activation criterion (30).
- The model capabilities have been assessed by comparing numerical simulations with experimental tests conducted on plain and holed strips of varying lengths under uniaxial tensile loading. The experimental results from the plain strips of different lengths have been used to calibrate the model constitutive parameters. This set of constitutive parameters has then been used to predict the response of the holed strips. A comparison between the model predictions and the experimental results has demonstrated, in most cases, a satisfactory accuracy regarding the reaction-displacement response curves, reflecting the dependence of the overall response on the relative orientation between material and loading directions. For the short-span specimens, the numerical curves for the 22.5°, 45°, and 67,5° material orientations resulted in a more brittle response than the corresponding experimental curves in the final part, close to specimen failure (good accuracy is obtained instead for the 0° and 90° orientations). On the other hand, the model has effectively captured the size effect, showing evident embrittlement in the case of long spans. A lower accuracy in predicting the displacement at the peak reaction force has been obtained in the case of the holed short-span specimen due to the increasing influence of the clamps when the length is decreased. As for the crack propagation path, the model has accurately reproduced the physical crack only for the 0° and 90° orientations, showing a limited sensitivity to the orientation with respect to the loading direction in the other cases. A factor that may possibly have introduced a bias in the crack propagation path is the artificial weakening that has been introduced in a thin central region of all specimens to trigger crack propagation far from the clamps.
- A limitation of the model is that only one value of fracture energy, the same in all material directions, can be defined. Since this affects only the final part of the response curve and experimental evidence shows that MD and CD fracture energies are, in general, rather similar, this does not affect the overall material response, dominated by the anisotropic plastic behavior. This may however have had an effect on the low sensitivity to material orientation of the crack propagation direction. An improvement of the model, aimed at overcoming this aspect, will be the object of future developments.

The proposed model does not cover the out-of-plane deformation of the board. This type of deformation is of great importance for the simulation of creasing and folding, which are key operations in the paperboard converting process. Since the anisotropy in the thickness direction is much higher than in the plane of the board, the extension of the proposed model is not straightforward and will be the object of future research.

CRediT authorship contribution statement

Alessandro Marengo: Writing – original draft, Validation, Software, Methodology, Investigation, Conceptualization. **Umberto Perego:** Writing – review & editing, Writing – original draft, Supervision, Methodology, Funding acquisition, Conceptualization. **Eric Borgqvist:** Writing – review & editing, Software. **Johan Tryding:** Writing – review & editing, Data curation. **Matti Ristinmaa:** Writing – review & editing, Supervision, Methodology.

Declaration of competing interest

The authors declare that they have no known competing financial interests or personal relationships that could have appeared to influence the work reported in this paper.

Data availability

No data was used for the research described in the article.

Acknowledgments

This work was partially supported by the Italian Ministry of University and Research (MUR) through the PRIN project XFAST-SIMS (No. 20173C478N). This support is gratefully acknowledged. Alessandro Marengo gratefully acknowledges the support by Innovhub and Tetra Pak Packaging Solutions.

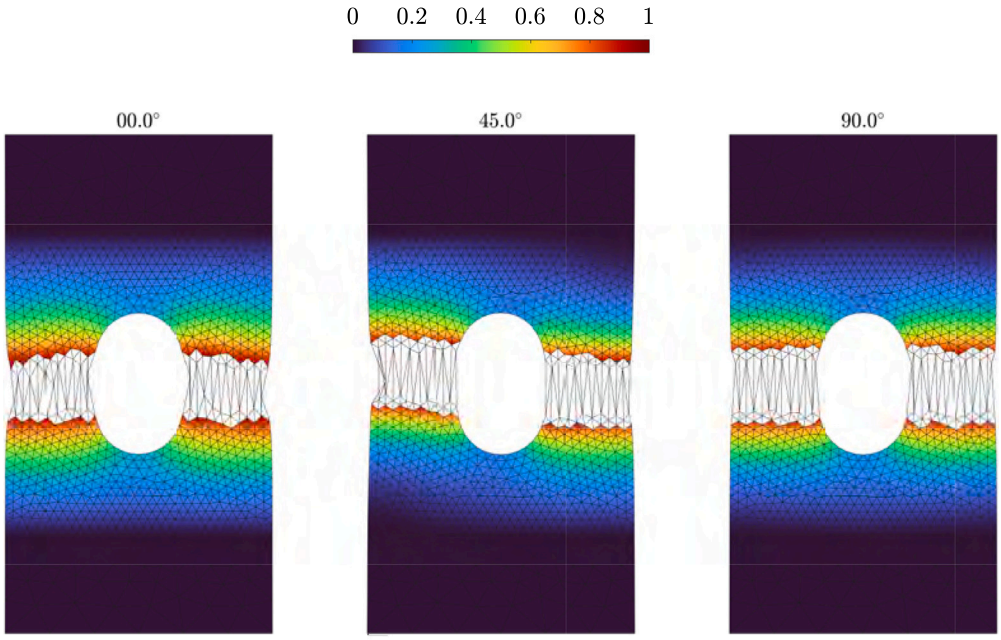

(a) Simulation

(b) Experimental

Fig. 13. Tensile test on paperboard holed strip. Short-span holed strip. Phase-field profile and experimental specimens at failure. Finite elements with $d \geq 0.95$ are shown in white.

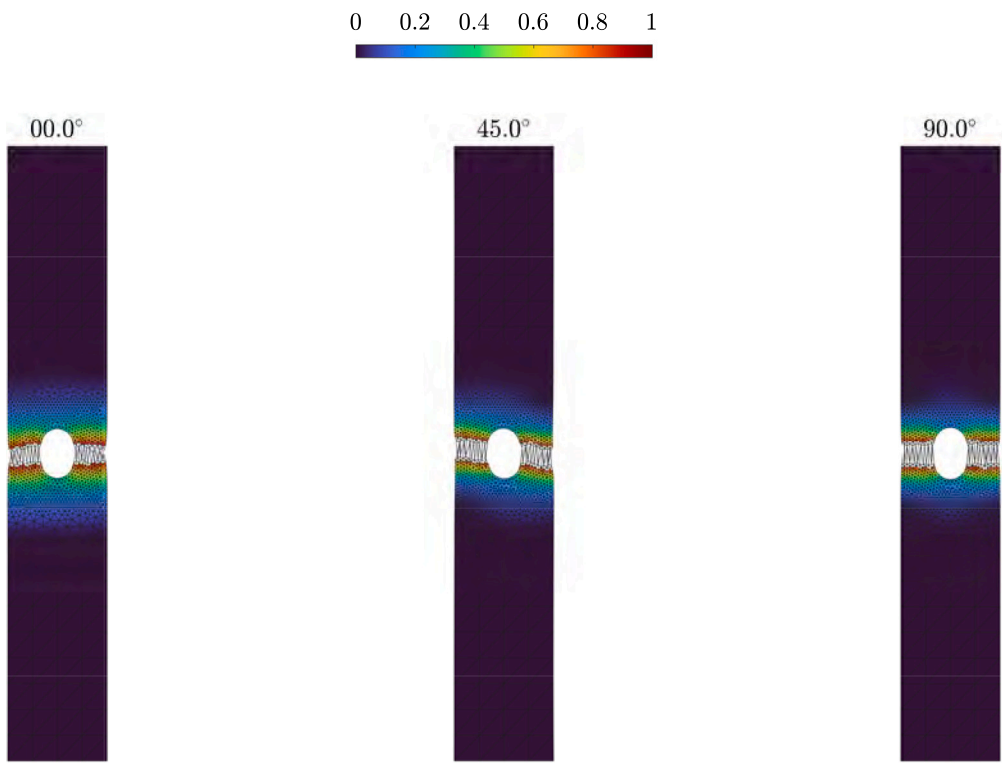

(a) Simulation

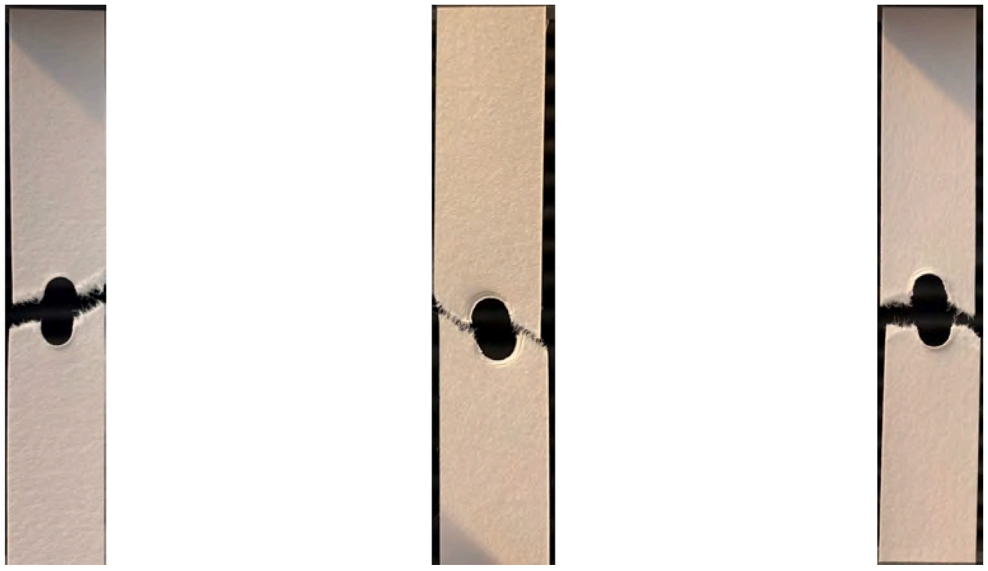

(b) Experimental

Fig. 14. Tensile test on paperboard holed strip. Long-span holed strip. Phase-field profile and experimental specimens at failure. Finite elements with $d \geq 0.95$ are shown in white.

References

Alessi, R., Ambati, M., Gerasimov, T., Vidoli, S., De Lorenzis, L., 2018a. Comparison of phase-field models of fracture coupled with plasticity. In: Oñate, E., Peric, D., de Souza Neto, E., Chiumenti, M. (Eds.), Advances in Computational Plasticity: A Book in Honour of D. Roger J. Owen. Springer International Publishing, Cham, pp. 1–21. http://dx.doi.org/10.1007/s00466-015-1151-4.

Alessi, R., Marigo, J.-J., Maurini, C., Vidoli, S., 2018b. Coupling damage and plasticity for a phase-field regularisation of brittle, cohesive and ductile fracture: one-dimensional examples. Int. J. Mech. Sci. 149, 559–576. http://dx.doi.org/10.1016/j.ijmecsci.2017.05.047.

Alzweighi, M., Tryding, J., Mansour, R., Borgqvist, E., Kulachenko, A., 2023. Anisotropic damage behavior in fiber-based materials: Modeling and experimental validation. J. Mech. Phys. Solids 181, 105430. http://dx.doi.org/10.1016/j.jmps.2023.105430.

Ambati, M., Gerasimov, T., De Lorenzis, L., 2015. Phase-field modeling of ductile fracture. Comput. Mech. 46, 1017–1040. http://dx.doi.org/10.1007/s00466-015-1151-4.

Ambrosio, L., Tortorelli, V., 1990. Approximation of functional depending on jumps by elliptic functional via Gamma-convergence. Comm. Pure Appl. Math. 43 (8), 999–1036. http://dx.doi.org/10.1002/CPA.3160430805.

Amor, H., Marigo, J.J., Maurini, C., 2009. Regularized formulation of the variational brittle fracture with unilateral contact: Numerical experiments. J. Mech. Phys.

Solids 57, 1209–1229. http://dx.doi.org/10.1016/j.jmps.2009.04.011.
Bleyer, J., Alessi, R., 2018. Phase-field modeling of anisotropic brittle fracture including several damage mechanisms. Comput. Methods Appl. Mech. Engrg. 336, 213–236. http://dx.doi.org/10.1016/j.cma.2018.03.012.
Borgqvist, E., Lindström, T., Tryding, J., Wallin, M., Ristinmaa, M., 2014. Distortional hardening plasticity model for paperboard. Int. J. Solids Struct. 51 (13), 2411–2423. http://dx.doi.org/10.1016/j.ijsolstr.2014.03.013.
Borgqvist, E., Wallin, M., Ristinmaa, M., Tryding, J., 2015. An anisotropic in-plane and out-of-plane elasto-plastic continuum model for paperboard. Compos. Struct. 126, 184–195. http://dx.doi.org/10.1016/j.compstruct.2015.02.067.
Borgqvist, E., Wallin, M., Tryding, J., Ristinmaa, M., Tudisco, E., 2016. Localized deformation in compression and folding of paperboard. Packag. Technol. Sci. 29 (7), 397–414. http://dx.doi.org/10.1002/pts.2218.
Bourdin, B., Francfort, G.A., Marigo, J.J., 2000. Numerical experiments in revisited brittle fracture. J. Mech. Phys. Solids 48, 797–826. http://dx.doi.org/10.1016/S0022-5096(99)00028-9.
Chen, N., Silberstein, M.N., 2019. A micromechanics-based damage model for non-woven fiber networks. Int. J. Solids Struct. 160, 18–31. http://dx.doi.org/10.1016/j.ijsolstr.2018.10.009.
Choo, J., Sun, W.C., 2018. Coupled phase-field and plasticity modeling of geological materials: From brittle fracture to ductile flow. Comput. Methods Appl. Mech. Engrg. 330, 1–32. http://dx.doi.org/10.1016/j.cma.2017.10.009.
Comi, C., Maier, G., Perego, U., 1992. Generalized variable finite element modeling and extremum theorems in stepwise holonomic elastoplasticity with internal variables. Comput. Methods Appl. Mech. Engrg. 96 (2), http://dx.doi.org/10.1016/0045-7825(92)90133-5.
Comi, C., Perego, U., 1995. A unified approach for variationally consistent finite elements in elastoplasticity. Comput. Methods Appl. Mech. Engrg. 121 (1), 323–344. http://dx.doi.org/10.1016/0045-7825(94)00703-P.
Comi, C., Perego, U., 1996. A generalized variable formulation for gradient dependent softening plasticity. Internat. J. Numer. Methods Engrg. 39, 3731–3755. http://dx.doi.org/10.1002/(SICI)1097-0207(19961115)39:21<3731::AID-NME24>3.0.CO;2-Z.
Comi, C., Perego, U., 2001. Fracture energy based bi-dissipative damage model for concrete. Int. J. Solids Struct. 38 (36–37), http://dx.doi.org/10.1016/S0020-7683(01)00066-X.
Corigliano, A., 1994. Numerical analysis of discretized elastoplastic systems using the generalized mid-point time integration. Eng. Comput. 11 (5), 389–411. http://dx.doi.org/10.1108/02644409410799353/FULL/XML.
Dean, A., Reinoso, J., Jha, N., Mahdi, E., Rolfes, R., 2020. A phase field approach for ductile fracture of short fibre reinforced composites. Theor. Appl. Fract. Mech. 106, 102495. http://dx.doi.org/10.1016/j.tafmec.2020.102495.
Domaneschi, M., Perego, U., Borgqvist, E., Borsari, R., 2017. An industry-oriented strategy for the finite element simulation of paperboard creasing and folding. Packag. Technol. Sci. 30 (6), http://dx.doi.org/10.1002/pts.2298.
Francfort, G.A., Marigo, J.J., 1998. Revisiting brittle fracture as an energy minimization problem. J. Mech. Phys. Solids 46 (8), 1319–1342. http://dx.doi.org/10.1016/S0022-5096(98)00034-9.
Gerasimov, T., De Lorenzis, L., 2019. On penalization in variational phase-field models of brittle fracture. Comput. Methods Appl. Mech. Engrg. 354, 990–1026. http://dx.doi.org/10.1016/j.cma.2019.05.038.
Giampieri, A., Perego, U., Borsari, R., 2011. A constitutive model for the mechanical response of the folding of creased paperboard. Int. J. Solids Struct. 48 (16–17), http://dx.doi.org/10.1016/j.ijsolstr.2011.04.002.
Hägglund, R., Gradin, P.A., Tarakameh, D., 2004. Some aspects on the zero-span tensile test. Exp. Mech. 44 (4), 365–374. http://dx.doi.org/10.1007/BF02428089.
Hagman, A., Nygårds, M., 2012. Investigation of sample-size effects on in-plane tensile testing of paperboard. Nord. Pulp Pap. Res. J. 27 (2), 295–304. http://dx.doi.org/10.3183/NPPRJ-2012-27-02-P295-304/MACHINEREADABLECITATION/RIS.
Halphen, B., Son, N.Q., 1975. On generalized standard materials. [Sur les materiaux standards generalises]. J. Mec. 14 (1), 39–63.
Harrysson, A., Ristinmaa, M., 2008. Large strain elasto-plastic model of paper and corrugated board. Int. J. Solids Struct. 45 (11–12), 3334–3352. http://dx.doi.org/10.1016/J.IJSOLSTR.2008.01.031.
Hu, T., Talamini, B., Stershic, A.J., Tupek, M.R., Dolbow, J.E., 2021. A variational phase-field model for ductile fracture with coalescence dissipation. Comput. Mech. 68, 311–335. http://dx.doi.org/10.1007/s00466-021-02033-1.
Huang, C., Gao, X., 2019. Development of a phase field method for modeling brittle and ductile fracture. Comput. Mater. Sci. 169, 109089. http://dx.doi.org/10.1016/j.commatsci.2019.109089.
Isaksson, P., Gradin, P., Kulachenko, A., 2006. The onset and progression of damage in isotropic paper sheets. Int. J. Solids Struct. 43 (3), 713–726. http://dx.doi.org/10.1016/j.ijsolstr.2005.04.035.
Isaksson, P., Hägglund, R., 2009. Structural effects on deformation and fracture of random fiber networks and consequences on continuum models. Int. J. Solids Struct. 46 (11), 2320–2329. http://dx.doi.org/10.1016/j.ijsolstr.2009.01.027.
Isaksson, P., Hägglund, R., Gradin, P., 2004. Continuum damage mechanics applied to paper. Int. J. Solids Struct. 41 (16), 4731–4755. http://dx.doi.org/10.1016/j.ijsolstr.2004.02.043.
Li, B., Maurini, C., 2019. Crack kinking in a variational phase-field model of brittle fracture with strongly anisotropic surface energy. J. Mech. Phys. Solids 125, 502–522. http://dx.doi.org/10.1016/j.jmps.2019.01.010.
Mäkelä, P., Östlund, S., 2003. Orthotropic elastic–plastic material model for paper materials. Int. J. Solids Struct. 40 (21), 5599–5620. http://dx.doi.org/10.1016/S0020-7683(03)00318-4.
Mangasarian, O., 1977. Solution of symmetric linear complementarity problems by iterative methods. J. Optim. Theory Appl. 22, 465–485. http://dx.doi.org/10.1007/BF01268170.
Marengo, A., Patton, A., Negri, M., Perego, U., Reali, A., 2021. A rigorous and efficient explicit algorithm for irreversibility enforcement in phase-field finite element modeling of brittle crack propagation. Comput. Methods Appl. Mech. Engrg. 387, 114137. http://dx.doi.org/10.1016/j.cma.2021.114137.
Marengo, A., Perego, U., 2023a. A concise review of small-strain phase-field modeling of ductile fracture. Eur. J. Mech. A Solids 105058. http://dx.doi.org/10.1016/J.EUROMECHSOL.2023.105058.
Marengo, A., Perego, U., 2023b. A small deformations effective stress model of gradient plasticity phase-field fracture. Comput. Methods Appl. Mech. Engrg. 115992. http://dx.doi.org/10.1016/j.cma.2023.115992.
Miehe, C., Aldakheel, F., Teichtmeister, S., 2017. Phase-field modeling of ductile fracture at finite strains: A robust variational-based numerical implementation of a gradient-extended theory by micromorphic regularization. Internat. J. Numer. Methods Engrg. 111, 816–863. http://dx.doi.org/10.1002/nme.5484.
Miehe, C., Hofacker, M., Welschinger, F., 2010. A phase field model for rate-independent crack propagation: Robust algorithmic implementation based on operator splits. Comput. Methods Appl. Mech. Engrg. 199, 2765–2778. http://dx.doi.org/10.1016/j.cma.2010.04.011.
Niskanen, K., Kettunen, H., Yu, Y., 2001. Damage width: a measure of the size of fracture process zone. In: The Science of Papermaking, Transactions of the 12th Fundamental Research Symposium, Oxford. FRC, Manchester, pp. 1467–1482.
Nygårds, M., Hallbäck, N., Just, M., Tryding, J., 2005. A finite element model for simulations of creasing and folding of paperboard. In: Abaqus Users' Conference. pp. 1–15.
Nygårds, M., Just, M., Tryding, J., 2009. Experimental and numerical studies of creasing of paperboard. Int. J. Solids Struct. 46 (11), 2493–2505. http://dx.doi.org/10.1016/j.ijsolstr.2009.02.014.
Ortiz, M., Martin, J.B., 1989. Symmetry-preserving return mapping algorithms and incrementally extremal paths: A unification of concepts. Internat. J. Numer. Methods Engrg. 28 (8), 1839–1853. http://dx.doi.org/10.1002/NME.1620280810.
Quintanas-Corominas, A., Reinoso, J., Casoni, E., Turon, A., Mayugo, J., 2019. A phase field approach to simulate intralaminar and translaminar fracture in long fiber composite materials. Compos. Struct. 220, 899–911. http://dx.doi.org/10.1016/j.compstruct.2019.02.007.
Raina, A., Miehe, C., 2016. A phase-field model for fracture in biological tissues. Biomech. Model. Mechanobiol. 15 (3), 479–496. http://dx.doi.org/10.1007/s10237-015-0702-0.
Robertsson, K., Borgqvist, E., Wallin, M., Ristinmaa, M., Tryding, J., Giampieri, A., Perego, U., 2018. Efficient and accurate simulation of the packaging forming process. Packag. Technol. Sci. 31 (8), 557–566. http://dx.doi.org/10.1002/pts.2383.
Samaniego, C., Ulloa, J., Rodríguez, P., Houzeaux, G., Vázquez, M., Samaniego, E., 2021. A phase-field model for ductile fracture with shear bands: A parallel implementation. Int. J. Mech. Sci. 200, 106424. http://dx.doi.org/10.1016/j.ijmecsci.2021.106424.
Simo, J.C., Honein, T., 1990. Variational formulation, discrete conservation laws, and path-domain independent integrals for elasto-viscoplasticity. J. Appl. Mech. 57 (3), 488–497. http://dx.doi.org/10.1115/1.2897050.
Simon, J.-W., 2021. A review of recent trends and challenges in computational modeling of paper and paperboard at different scales. Arch. Comput. Methods Eng. 28 (4), 2409–2428. http://dx.doi.org/10.1007/s11831-020-09460-y.
Stenberg, N., Fellers, C., 2002. Out-of-plane Poisson's ratios of paper and paperboard. Nord. Pulp Pap. Res. J. 17 (4), 387–394. http://dx.doi.org/10.3183/npprj-2002-17-04-p387-394.
Talamini, B., Tupek, M.R., Stershic, A.J., Hu, T., Foulk, J.W., Ostien, J.T., Dolbow, J.E., 2021. Attaining regularization length insensitivity in phase-field models of ductile failure. Comput. Methods Appl. Mech. Engrg. 384, 113936. http://dx.doi.org/10.1016/j.cma.2021.113936.
Teichtmeister, S., Kienle, D., Aldakheel, F., Keip, M.-A., 2017. Phase field modeling of fracture in anisotropic brittle solids. Int. J. Non-Linear Mech. 97, 1–21. http://dx.doi.org/10.1016/j.ijnonlinmec.2017.06.018.
Ulloa, J., Rodríguez, P., Samaniego, E., 2016. On the modeling of dissipative mechanisms in a ductile softening bar. J. Mech. Mater. Struct. 11 (4), 463–490. http://dx.doi.org/10.2140/JOMMS.2016.11.463.
Wambacq, J., Ulloa, J., Lombaert, G., François, S., 2021. Interior-point methods for the phase-field approach to brittle and ductile fracture. Comput. Methods Appl. Mech. Engrg. 375, 113612. http://dx.doi.org/10.1016/j.cma.2020.113612.
Xia, Q.S., Boyce, M.C., Parks, D.M., 2002. A constitutive model for the anisotropic elastic–plastic deformation of paper and paperboard. Int. J. Solids Struct. 39 (15), 4053–4071. http://dx.doi.org/10.1016/S0020-7683(02)00238-X.
Yin, B., Kaliske, M., 2020. A ductile phase-field model based on degrading the fracture toughness: Theory and implementation at small strain. Comput. Methods Appl. Mech. Engrg. 366, 113068. http://dx.doi.org/10.1016/j.cma.2020.113068.